External Object Detection in Wireless Power Transfer for EV

Adilkhan Kapanov, B.Eng. in Electrical and Computer Engineering

Submitted in fulfilment of the requirements

for the degree of Master of Science

in Electrical and Computer Engineering

School of Engineering and Digital Sciences

Department of Electrical and Computer Engineering

Nazarbayev University

53 Kabanbay Batyr Avenue,

Nur-Sultan, Kazakhstan, 010000

Supervisor: Mehdi Bagheri

Co-supervisor: Annie Ng

11.04.2025

DECLARATION

I hereby, declare that this manuscript, entitled “External Object Detection in Wireless Power Transfer for EV”, is the result of my own work except for quotations and citations which have been duly acknowledged.

I also declare that, to the best of my knowledge and belief, it has not been previously or concurrently submitted, in whole or in part, for any other degree or diploma at Nazarbayev University or any other national or international institution.

Name: Adilkhan Kapanov

Date: 20.03.2025

Abstract

Wireless power transfer (WPT) is short-distance magnetic coupling between transmitter and receiver coils that allows electrical energy to be transferred without a direct wired connection, which consequently offers a safer environment. However, there are serious risks associated with external metallic objects (EMOs) in the system's operating area, such as the possibility of causing fire from overheating brought on by eddy currents. By putting forth a unique sensing coil-based External Object Detection (EOD) technique, this thesis tackles the crucial problem of EMO detection. The method uses five open-circuited single-turn sensor coils to track changes in electromagnetic parameters brought on by EMO-induced eddy currents, including resistance, mutual inductance, and self-inductance. The technique ensures safety prior to high-power charging in WPT system specifically for EVs by assessing these variations and accurately identifying EMOs while running at pre-startup power levels.

In order to assess the system's reaction to various EMO scenarios, such as different shapes (such as coins, cans, and spoons), sizes, and frequency spectrum, the research combines mathematical modeling with Finite Element Analysis (FEA) simulations using Ansys Electronics Desktop. The method's robustness is confirmed by experimental validation, which was carried out over a frequency range of 80-90 kHz and shows strong detection accuracy under misalignment settings. Reliable detection of EMOs is made possible by the results, which reveal sequent error values below 1 % in EMO-free situations and escalating to 3-12 % in EMO-present cases.

The study also investigates EMO localization via spatial error mapping, demonstrating increased sensitivity at higher elevations and central locations. The transmitter-side exclusivity and power-level invariance of the suggested approach make it easier to deploy in stationary EV charging infrastructure. This work enhances the practical deployment of WPT systems by improving safety and reliability, opening the door for wider implementation in sustainable transportation. To further enhance dynamic performance, future developments might incorporate hybrid sensing approaches or machine learning for adaptive calibration.

Table of Contents

Abstract 2
List of Abbreviations. 4
List of Figures. 5

Chapter 1 – Introduction. 9
1.1 Background. 9
1.1.1 Far-Field WPT. 9
1.1.2 Near-Field WPT. 9
1.1.2.1 Capacitive Power Transfer (CPT). 9
1.1.2.2 Resonant-Coupled Inductive Power Transfer (RC-IPT) 10
1.2 Problem Definition. 11
1.3 Aims and Objectives 12
1.4 Thesis outline 13

Chapter 2 – Literature Review. 14
2.1 Living Object Detection (LOD) 14
2.2 Metal Object Detection (MOD) 14
2.2.1 Parameter-Based Method. 14
2.2.2 Sensing Coil-Based Method. 16
2.2.3 Sensor-Based Method. 18
2.2.4 Comparison of MOD Methods 20

Chapter 3 – Research Methodology and Modelling 22
3.1. WPT-EOD Method. 22
3.2. Modelling of WPT-EOD System 23
3.3. Finite Element Analysis on the Effects of EMO on the WPT-EOD System. 33

Chapter 4 – Experimental Study. 44
4.1. Information on the setup. 44
4.2. Measurement of Coil Parameters 46
4.3. MOD at Constant Current and Constant Input Power Cases. 49
4.4. Localization of the EMO. 51

Chapter 5 – Discussion 54
4.1. Information on the setup. 54
4.2. Measurement of Coil Parameters 54
4.3. MOD at Constant Current and Constant Input Power Cases. 55

Chapter 6 – Conclusion and Future Work 56

References/Bibliography. 58

List of Abbreviations

WPT	Wireless power transfer
IPT	Inductive power transfer
CPT	Capacitive power transfer
RC-IPT	Resonant coupled inductive power transfer
EV	Electric vehicle
EO	External object
MO	Metallic object
LO	Living object
EMO	External metallic object
ELO	External living object
EOD	External object detection
MOD	Metallic object detection
LOD	Living object detection
FEA	Finite element analysis
ECP	Equivalent circuit parameter
Tx	Transmitter coil

List of Figures

Figure 1.1: External metal object in the WPT system for an EV. 11

Figure 2.1: Schematic of the eddy current effect of a metal object in WPT systems. 15

Figure 2.2: Schematic of the implementation of the sensing coil in WPT systems. 17

Figure 2.3: Sensor-based MOD in WPT systems. 19

Figure 3.1: Schematic model and structure of the WPT-EOD system. 24

Figure 3.2: Equivalent electrical circuit of proposed resonant coupled wireless power transfer system with five sensing coils and external object. 25

Figure 3.3: Four simulation cases in Ansys Electronics Desktop. 34

Figure 3.4: Simulation setup of the case 4 in the Ansys Electronics Desktop. 35

Figure 3.5: Self-inductance of (a) Transmitter coil, (b) S1 coil, (c) S2 coil, (d) S3 coil, (e) S4 coil, and (f) S5 coil over the range of frequency from 10 kHz to 1 MHz. 36

Figure 3.6: Self-resistance of (a) Transmitter coil, (b) S1 coil, (c) S2 coil, (d) S3 coil, (e) S4 coil, and (f) S5 coil over the range of frequency from 10 kHz to 1 MHz. 37

Figure 3.7: Self-inductance of (a) Transmitter coil, (b) S1 coil, (c) S2 coil, (d) S3 coil, (e) S4 coil, and (f) S5 coil over the range of frequency from 80 kHz to 90 kHz. 38

Figure 3.8: Self-resistance of (a) Transmitter coil, (b) S1 coil, (c) S2 coil, (d) S3 coil, (e) S4 coil, and (f) S5 coil over the range of frequency from 80 kHz to 90 kHz. 39

Figure 3.9: Sequent error results of the four simulation cases over the range of frequency from 10 kHz to 1 MHz. 41

Figure 3.10: Sequent error results of the four simulation cases over the range of frequency from 80 kHz to 90 kHz. 42

Figure 4.1: The experimental setup of the proposed system:1) power supply; 2) inverter; 3) coil setup; 4) rectifier; 5) electronic load; 6) oscilloscope. 44

Figure 4.2: Four experimental cases for the experimental setup. 45

Figure 4.3: Coil setup of the proposed EOD method: 1) transmitter coil; 2) five open-circuited sensing coils; 3) space for EMO; 4) receiver coil 46

Figure 4.4: Experimental measurement of self-inductance of (a) Transmitter coil, (b) S1 coil, (c) S2 coil, (d) S3 coil, (e) S4 coil, and (f) S5 coil over the range of frequency from 80 kHz to 90 kHz. 47

Figure 4.5: Experimental measurement of self-resistance of (a) Transmitter coil, (b) S1 coil, (c) S2 coil, (d) S3 coil, (e) S4 coil, and (f) S5 coil over the range of frequency from 80 kHz to 90 kHz. 48

Figure 4.6: Sequent error results of the four experimental cases over the range of frequency from 80 kHz to 90 kHz at 2 A transmitter current 50

Figure 4.7: Sequent error results of the four experimental cases over the range of frequency from 80 kHz to 90 kHz at 10 W input power 51

Figure 4.8: Different measuring points of the experimental setup for the localization purposes. . .52

List of Tables

Table 2.1: The comparison of MOD methods. 20

Table 4.1: The sequent error values at different points of the experimental setup. 52

Chapter 1 – Introduction

1.1 Background

Transferring energy from a single source to the load without the use of wires is known as wireless power transfer (WPT). There are two types of WPT: far-field WPT or microwave power transfer and near-field WPT [1, 2].

1.1.1 Far-Field WPT

Far-field WPT techniques, also known as microwave power transfer, are a type of power transmission technique in which information and power are transmitted using radio waves whose wavelengths fall within the microwave category. A microwave generator, receiving antenna, and transmitting antenna make up microwave power transfer system. In microwave WPT, there is no magnetic coupling between the transmitting and receiving antennas. The main drawback of microwave power transfer is its high-power transmission, which is unsafe for people and does not comply with high power radio wave regulations [3, 4]. However, due to its working principle, far-field WPT systems advantage relies on its charging distance which can be realized in the cases of transferring energy from solar power satellite in space to the ground [5].

1.1.2 Near-field WPT

Near-field WPT techniques use electric fields with capacitive coupling between electrodes and magnetic fields with inductive coupling between coils to transfer power over short distances.

1.1.2.1 Capacitive Power Transfer (CPT)

In CPT systems the transmitter and receiver coils are made up of two pairs of metal plates that make up the coupling medium [6]. An appropriate insulator or dielectric is applied to the connection plates. The plates have the appearance of a capacitor that is loosely connected. Bipolar and unipolar capacitive interfaces are the two varieties [7]. An electric field forms between the transmitter and receiver side plates of the capacitor when electrical energy is applied to the transmitter plate. A displacement current flows between the transmitter and receiver as a result of the electric field. An equivalent series resistance and an equivalent series inductance make up the capacitive interface. The self-resonant frequency of the coupling capacitor is the frequency at which the corresponding internal series inductance creates a series resonant circuit [8]. The benefit of resonance is that it allows for maximum power flow, and resonating parts let the fundamental component flow while acting as a filter to exclude higher order harmonics. Because capacitive power transfer systems are resonant in nature and have a major advantage over inductive power transfer systems in reducing electromagnetic interference (EMI), the converters in these systems operate in either zero voltage switching (ZVS) or zero current switching (ZCS), which makes them incredibly efficient [9].

1.1.2.2 Resonant-Coupled Inductive Power Transfer (RC-IPT)

Inductive Power Transfer (IPT) is the process of transferring power through magnetic fields. The primary coil's alternating current generates an alternating current on the receiver coil side [10, 11].

Since it employs strongly coupled magnetic resonance, RC-IPT is an enhanced version of IPT that performs best over midrange distances when compared to other WPT techniques. Because the magnetic flux density in IPT decreases quickly along the range gap, power transferring

efficiency decreases at a rate that is a cubic of the distance between coils [12]. To address these issues, the highly resonant WPT approach is useful because it uses the resonant coupling to strengthen standard induction. The capacitor can be used in the system to minimize the amount of reactance and maximize the power transmission capacity [13]. The primary determinant of this method's overall performance is the quality factor, which is inversely proportional to the circuit's capacitance, consequently meaning the smaller the capacitance, the higher the overall efficiency becomes [14, 15].

1.2 Problem Definition

WPT systems have their own problems that need to be fixed even though they offer a safer environment. One of the problems is when an external object (EO), like keys, coins, or tiny animals, is present in the system's operating area. Due to the working conditions of the system, which include high power levels and the presence of strong AC electromagnetic fields between coils, the presence of EO may lead to potentially dangerous situations. External metal objects (EMOs) and external living objects (ELOs) are the two types of EO. While the presence of LOs can lead to blood pressure issues or vertigo, the presence of EMOs in the system can result in fire hazards [16].

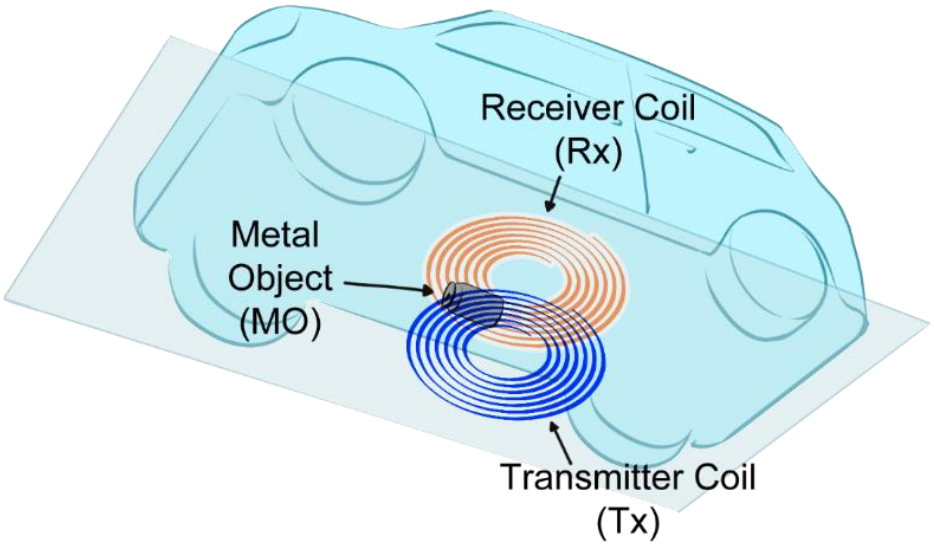

Figure 1.1: External metal object in the WPT system for an EV

External object detection (EOD) techniques are being researched to stop these situations. Metal object detection (MOD) and living object detection (LOD) are two types of EOD techniques that are based on the physical characteristics of the object [17]. The goal of MOD techniques is to locate metallic objects within the system's operating space. These techniques fall into three primary categories: sensor-based, sensing coil-based, and parameter-based. The three MOD approaches were compared in a study by [18]. The parameter-based approach, which has the advantage of not requiring extra equipment or costs and having a longer detection time than other approaches, works by examining changes in the system's own parameters. However, it is inapplicable in high-power applications, which is a critical component for EVs, and its efficacy declines in misalignment situations. The lack of a proven sensing coil design that will function regardless is the only drawback of the sensing coil-based approach, which can detect EMOs in misalignment situations and run at high power levels when compared to the parameter-based approach. Lastly, the sensor-based approach offers better accuracy and identification in misalignment situations due to its

reliance on external sensors. To accurately identify EMO, it also necessitates higher costs and reliance on the operating environment. Since LOD techniques use a CPT system to identify LOs that is inappropriate for this project's situation, they cannot be targeted EOs in this project. The use of the sensor-based approach to EOD is another factor.

1.2 Aims and Objectives.

This research study proposes sensing coil-based method of external object detection and its sensitivity analysis over the range of frequencies. The project aims to provide important insights for the creation of future WPT systems that can function reliably and effectively in dynamic frequency situations by tackling these goals.

1.3 Thesis Outline

First, the thesis project aims to achieve the visualization of how EMOs affect the original magnetic flux distribution and to investigate the induced eddy currents over the EMOs by employing FEA. FEA technique is performed using Ansys Electronics Desktop software on the system with different cases considering different shapes and types of EMO at the frequency range from 10 kHz to 1 MHz and from 80 kHz to 90 kHz. Thus, the effects on the transferring efficiency and the variation of self- and mutual-resistances and inductances are analyzed across the frequency band. For the proposed WPT-EOD system an equivalent electrical circuit with and without presence of EMO is derived. By applying matrix reduction method, the effects of the EMO are shown on the base system parameters. A thorough analysis of both the original and modified ECPs is conducted. Finally, the accuracy of the proposed EOD technique is going to be validated by fabricating an experimental setup. Additionally, the localization of the EMO from the experimental setup measurements are carried out.

Chapter 2 – Literature Review

2.1 Living Object Detection (LOD)

The LOD technique is a significant component of EOD, as it can negatively impact living organisms, including humans, by inducing dizziness, altering blood pressure, and disrupting organ function [18]. The LOD method in [19] is based on two sensors that detect the presence of LO in the system by measuring ultrasonic distances. Increased reliability necessitates the incorporation of more sensors. An alternative approach to discover LOs inside the system is to employ a distinct sort of WPT system, specifically a CPT system. In [20], resonance CPT was introduced, demonstrating the system's capability to identify living tissue under simulated settings.

2.2 Metal Object Detection (MOD)

The goal of MOD techniques is to locate MO within the system's working region. These techniques fall into three primary groups: parameter-based, sensing coil-based, and sensor-based.

2.2.1 Parameter-Based Method

Eddy currents are produced in the MOs located in the area between the transmitter and reception coils, which is loaded with powerful AC magnetic fields. Eddy currents in MOs then produce a new magnetic field that is opposite to the transmitter coil's initial magnetic field. Furthermore, the existence of MOs in the system alters a number of electrical properties, including the impedances of the transmitter and reception coils. These variables include coil quality factor, voltage, current, and transfer efficiency. MOs can be identified by monitoring and evaluating changes in these parameters [18]. The subsequent figure depicts the influence of the MOs, where I_{eddy}, B_0, and B_m denote the eddy currents generated in the MO, the original magnetic field, and the counteracting magnetic field produced by the MO, respectively:

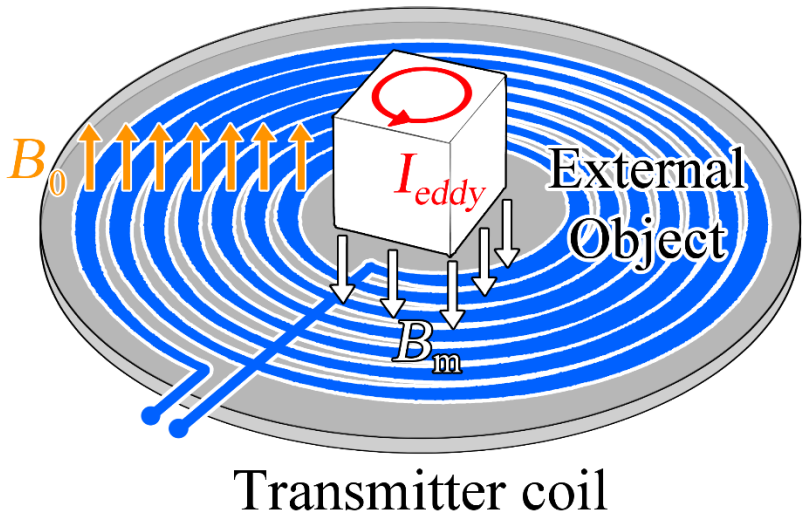

Figure 2.1: Schematic of the eddy current effect of a metal object in WPT systems

Recent works on the parameter-based method has increasingly employed algorithms, classifiers, and various methodologies to enhance the analysis of fluctuating parameters inside the system influenced by EOs. The analytical computation of impedance variation on the transmitter side of the system, utilizing high-frequency excitation from an auxiliary supporting circuit, was introduced in a work by [21], which encompasses both offline and online methods of MO detection. The offline approach detects without utilizing the receiver side of the device, while the online method detects MO using both coils. Consequently, in both instances, minor molecular orbitals were discernible when the excitation frequency precisely matched the self-resonant frequency of the system. A long short-term memory classifier utilizing a feature extraction method is employed to detect the existence of the MO in the system by analyzing 298 signals obtained from measurements of the transmitter inverter current. The findings indicate a 95 % accuracy of the EOD method. Another method outlined in [22] employed dual frequency tuning for detection, aiming to maintain a low detection current, hence enhancing system power efficiency. While the proposed approach can efficiently detect MO, the distance between coils and the overall dimensions of the

system are unsuitable for practical applications. A unique method for applying bifurcation to a system, which measures the peak amplitudes of currents on the primary side at the resonant frequency to detect MOs, is detailed in [23]. The authors state that the suggested method is more trustworthy than other alternatives, as it relies solely on measurements from the transmitter side and operates under bifurcation phenomena. The study in [24] presents a real-time enhancement of the EOD approach with a PSO algorithm, incorporating a fitness function that evaluates both projected and actual measurement outcomes from voltage and current readings on the primary side. The method offers two metrics: one assesses the presence of MOs, while the other measures their influence on the system. The primary influence on the system comprises a copper plate, an iron coin, and a copper coin.

2.2.2 Sensing Coil-Based Method

Currently, the most widespread and extensively discussed MOD technique is the sensing coil-based approach. Because MO alters the magnetic field in the system, its presence can be detected by measuring the induced voltage's parameters at the sensing coil. Because it uses changes in magnetic fields to detect EMOs, this technique is also known as the field-base method. This approach can be divided into three subcategories: combined, active, and passive. The passive approach, which is limited to the resources that the system initially provided, uses the transmitter coil's generated voltage in the sensing coil and no external power sources to detect EMOs. Passive systems, however, are unable to detect MOs prior to the transmission process. However, by employing external power sources, the active method is able to excite the sensing coil and identify EMOs prior to the transmission process. Both approaches are used in the combined method [18].

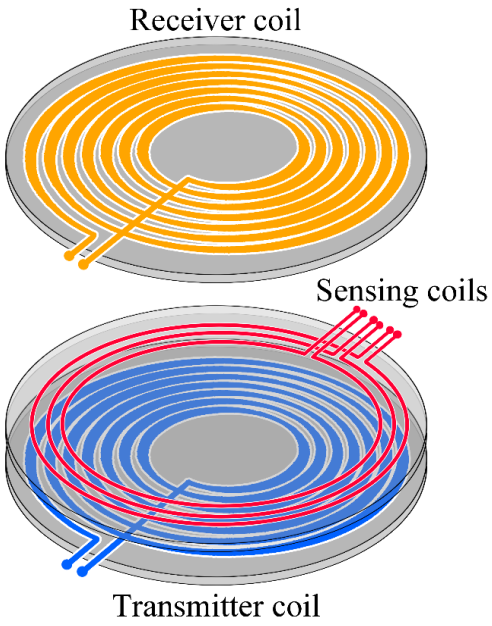

Figure 2.2: Schematic of the implementation of the sensing coil in WPT systems

Even though this approach is widely used, the following problems are still present when looking at the state of the art: The presence of blind areas on the sensing coils, where EMO identification is impossible due to environmental, design, and positioning issues: 1. Parking position or misalignment of both coils may make it difficult for the sensing coil in the system to identify EMOs; 2. Expand the scope of the experimental tests by considering the EMOs in addition to the changing parameters of the sensing coils; 3. The lack of universal assessment or testing procedures [25].

Sensing coils positioned perpendicular to the transmitter coil is a recently proposed technique that solves the aforementioned problem [26, 27]. The following are some benefits of the suggested design: By adding short sensing coils to the system, it: 1) eliminates blind areas; 2) maintains detecting accuracy in cases of misalignments between the main system coils; and 3) provides decoupling between the sensing coil and the main system coils. Because the sensing coils

are made as a two-layer PCB, the method is therefore economical. The MOD algorithm proposed in [28], which is based on multivariate normal distribution, greatly enhances the ability to detect EMOs in the corner sections of the detection coil when compared to conventional detection techniques. A 19 mm dime was used to test the system configuration. Eight small, simple sensor coils are wound around the transmitting coil in [29] in order to identify and locate EMOs. The change in mutual inductance between each sensing coil and transmitter coil is then detected. The EMO position on the space was determined in the experimental setup, and it was found that the presence of the EMO alters mutual inductance by 40-80 %. Feature extraction from a self-excited oscillation circuit is the basis of another suggested MOD technique [30]. Compared to other geometric coil designs, the suggested method's single rectangular coil offers superior detection accuracy and dependability. Following six experimental configurations with various EMO locations within the system, in the work of [30] it was determined that establishing particular threshold detection ranges of frequency and amplitude differences can result in a practical MOD technique. This thesis project was primarily inspired by another study of [31], which measured the deviation from a standard electromagnetic model caused by EMO in the system using MOD. The suggested method works at different detection power levels and can handle coil misalignment situations up to 10 cm.

2.2.3 Sensor-Based Method

The sensor-based MOD technique primarily employs additional sensor devices, complicating system design but facilitating accelerated and broader detection capabilities [18].

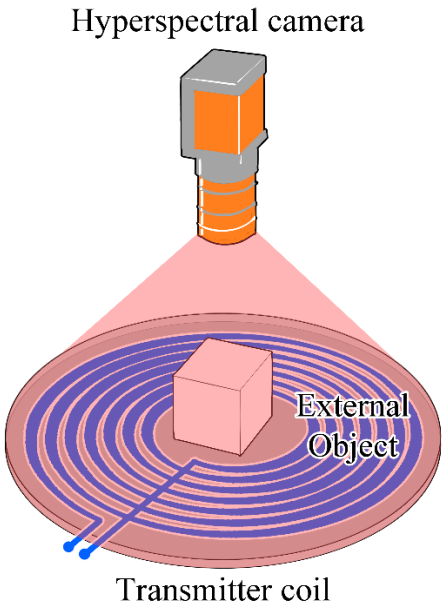

Figure 2.3: Sensor-based MOD in WPT systems

The present study on this technique showcases an integration of hardware sensors and machine learning algorithms that enhance overall efficacy. In [32], he proposed the safeguarding of living entities and explosive ordnance disposal within a wireless power transfer system utilizing a singular sensor, a FLIR Lepton thermal camera, alongside several deep learning models to evaluate system enhancement and performance. The simulated human hand was reliably detected; nevertheless, enhancements in subsequent actions were still necessary. MOs were identified in 35 milliseconds at safe temperature levels, allowing human contact without risk of injury. The identical idea was utilized in [33], whereby a thermal infrared image sensor, an ARM microcontroller, and image processing methodologies were employed in the proposed system. MOs as large as half a coin were recognized at a distance of 15 cm within 0.5 seconds, with a temperature differential of 7 °C between the MO and the background being adequate for detection. A distinct methodology employing hyperspectral imaging techniques and machine learning is proposed in [34]. The proposed technique can differentiate MOs in the system due to the distinct features of

each material. The system achieves a 100 % recognition rate for MOs, including its capacity to detect small-sized items.

2.2.4 Comparison of MOD Methods

Following an examination of recent research on the three MOD approaches, an overview of their operational principles, advantages, and disadvantages is provided in Table 2.1:

Table 2.1. The comparison of MOD methods.

MOD methods	**Operating principle**	**Advantages**	**Disadvantages**
Parameter-based	Examining the electrical properties of the system resulting from variations in the self-inductance of the coils	• The system is self-sustaining, necessitating no supplementary equipment or costs; • High detection time.	• Challenging to recognize MOs in misalignment situations; • Inappropriate for high-power applications.
Sensing coil-based	Through the examination of the induced voltage, induced current, and impedance of the sensing coil	• Tolerance for misalignment; • Capability to detect small-sized MOs; • Functions at various power levels.	• Necessity for consistent design to eradicate blind spots.
Sensor-based	Assess or observe variations in the physical characteristics of a system utilizing external sources.	• Extensive detection range; • Functions effectively despite misalignment; • High accuracy.	• Elevated costs compared to alternatives; • Performance impacted by external factors; • Complexity in circuit implementation due to size.

Table 2.1 illustrates a comparison of the three MOD approaches. The parameter-based technique functions by examining variations in the system's characteristics, offering benefits such

as the absence of supplementary equipment and costs, as well as enhanced detection time relative to alternative methods. Nonetheless, its efficacy diminishes in instances of misalignment and is inapplicable in high-power applications, a critical consideration for electric vehicles. The sensing coil-based approach, in contrast to the parameter-based method, can detect MOs in misalignment scenarios and functions at elevated power levels; nevertheless, its sole drawback is the lack of a universally applicable sensing coil design. Ultimately, due to its reliance on external sensors, the sensor-based approach offers enhanced precision and diagnosis in instances of misalignment. Nonetheless, it necessitates more expenses and reliance on the operational environment to accurately diagnose MO.

The comparison between LOD and MOD methods is not conducted since LOD employs a different sort of WPT system, specifically CPT, in contrast to MOD methods. In all MOD techniques, the system functions based on IPT.

Chapter 3 – Research Methodology and Modelling

3.1 WPT-EOD Method

In this thesis work, Electromagnetic EOD method applying five open-circuited single-turn sensing coils to modify existing transmitter current is utilized. In this regard, geometric parameters and sense coil voltages, which capture the electromagnetic couplings between the transmitter, receiver, and sense coils are necessary for the modification. When an external object is present, the transmitter coil current modification becomes inaccurate due to emerging of a sequent error caused by the geometric parameters not having the additional coupling from the eddy winding in the foreign object. The sequent error, which arises from a foreign object due to additional electromagnetic coupling, is useful as a detection metric. The genuine Tx coil current is measured independently and compared to the reconstructed Tx coil current [31, 35].

The main reason for choosing Electromagnetic EOD method applying five open-circuited single-turn sensing coils as the main method for the project was because of its advantages over other methods, such as:

1) Power level invariance, leading to the low-power startups before charging EV.

2) The ability to identify EMOs in the cases of lateral misalignment up to 10 cm.

3) The ability to detect EMOs within the operating area of the system with no blind areas.

4) Reliance only on the transmitter side of the system.

The proposed method suggests utilizing five sensing coils to accurately perform EOD. The efficiency of the proposed method is maintained by the employment of five sense coils, which allows the system to precisely modify the transmitter coil current even in the cases of misalignment up to 10 cm with receiver coil, leading to successfully reducing the sequent error that may arise

from such cases. The inclusion of more sensing coils in the system would result in insignificant increment performance of the system.

The pre-startup power level of 10W was selected for the purpose of identification of EMOs. The system may safely scan for EMOs at this power level without subjecting them to the high-power levels, which are required for properly charging EVs. Due to invariance to the operating power levels, this characteristic gives an opportunity to identify EMOs safely without causing any risks to the system.

Because of its stationary nature and benefits it provides for identifying EMOs in a WPT system, the transmitter coil was selected for measurement. In WPT systems, like EV charging stations, no one have an access to the transmitter coil, which is stationary. Additionally, because the receiver coil may move or misalign while in use, using only the transmitter coil removes the requirement to measure or access it. Since just the transmitter coil's characteristics and sensing coil voltages need to be monitored, this simplifies and strengthens the system architecture.

3.2 Modelling of WPT-EOD System

Figure 3.1 shows a schematic of the proposed WPT-EOD system studied in [31]. Series-series topology, that connects single capacitor in series to a magnetic coil at both transmitter and receiver side is used due to its widespread usage in IPT systems [36]. The first part of the system consists of a voltage source from which the main power is distributed and an inverter that converts DC from the source into AC. In the second part of the system, transmitter coil is present with its corresponding compensating capacitor. The third part consists of five single-turn open-circuited sensing coils. Next part is the receiver part that consists of receiver coil and its corresponding compensating capacitor. In the fifth part, rectifier is present which transforms incoming AC into DC. In the last part of the system, the converted DC starts to charge the battery by passing through

the noise filter created by the capacitor and inductor. Between sensing coils and receiver parts EMO is placed.

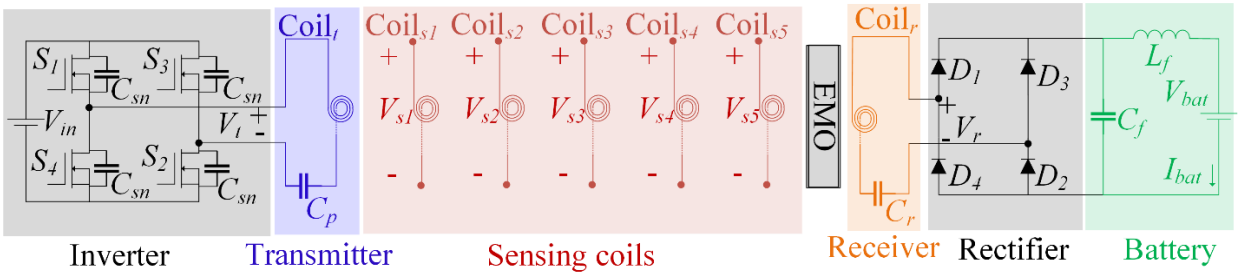

Figure 3.1: Schematic model and structure of the WPT-EOD system

The planar spiral coil design was selected as the primary design because of its widespread use [37]. Note that Litz wires, namely the skin effect, reduce AC winding losses, which is the reason they employed rather than a single solid wire. The phenomenon known as the "skin effect" occurs when most AC current running through a wire is carried on its surface rather than in the cross-sectional center, leaving only a tiny amount of current in the wire's core [38].

Transmitter coil is chosen as the reference for the current measurement to track the main changes in the system due to the fact that, in the system of EV wireless charging, transmitter coil remains stationary and close to the sensing coils, which lead to a more accurate result.

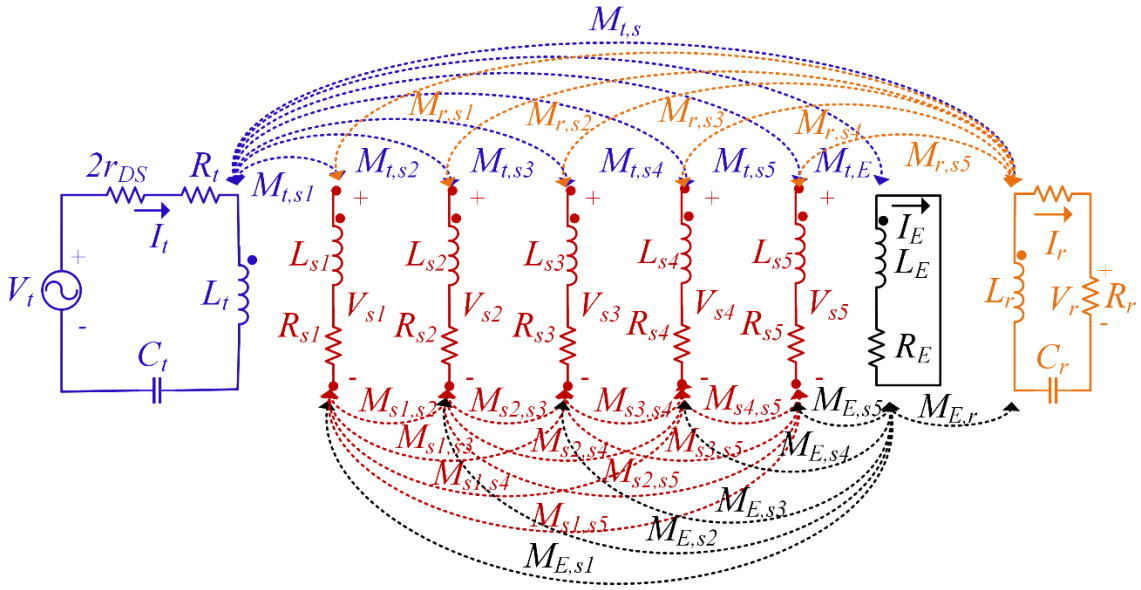

Figure 3.2: Equivalent electrical circuit of proposed resonant coupled wireless power transfer system with five sensing coils and external object

Configuration and basic schematics of the studied WPT-EOD system are shown in Figure 3.1, while the equivalent electronic circuit depicting the components and variables of the system operating at 85 kHz is shown in Figure 3.2. R_t and R_r are the resistance, L_t and L_r are the self-inductance, and C_t and C_r are the compensating capacitor of the transmitter and receiver magnetic coils. EMO is modeled by an equivalent eddy current circuit which has also couplings with other magnetic coils and sense coils and includes a self-inductance and resistance respectively denoted by L_E and R_E. Additionally, each sense coils have a self-inductance of L_{sx} and resistance R_{sx}, where x refers to each of the five sense coils. The mutual inductance between the transmitter and receiver magnetic coils and external object is denoted as $M_{t,E}$ and $M_{r,E}$. As for the mutual inductance between transmitter and the open-circuited sense coil voltages can be denoted as $M_{t,s1}$, $M_{t,s2}$, $M_{t,s3}$, $M_{t,s4}$, and $M_{t,s5}$. The mutual inductance between receiver and the open-circuited sense coil voltages can be denoted as $M_{r,s1}$, $M_{r,s2}$, $M_{r,s3}$, $M_{r,s4}$, and $M_{r,s5}$. The mutual inductance between EMO and

sense coil voltages are $M_{E,s1}$, $M_{E,s2}$, $M_{E,s3}$, $M_{E,s4}$, and $M_{E,s5}$. Lastly, the mutual inductance between each of sensing coils with each other denoted as $M_{s1,s2}$, $M_{s1,s3}$, $M_{s1,s4}$, $M_{s2,s3}$, $M_{s2,s4}$, $M_{s2,s5}$, $M_{s3,s4}$, $M_{s3,s5}$, and $M_{s4,s5}$.

The inverter voltage (V_t) displayed on the transmitter side is generated by applying a half-cycle at a designated duty cycle for both switching pairs of the inverter's diodes, [S1, S2] and [S3, S4], and may be expressed as $V_t = (4/\pi)V_{in}\angle 0°$, where V_{in} is the DC link voltage of the inverter. The formula for the inverter current (I_t) is $I_t = |I_t|\angle -\theta_{in}$, where $|I_t|$ is the current magnitude and θ_{in} is the inverter system's input impedance angle. Furthermore, Fig. 4 shows the conducting resistance of the inverter's switching diodes as $2r_{DS}$.

At the receiver side, the voltage and current at the rectifier terminal are expressed as $V_s = (4/\pi)(V_{bat} + 2V_D)\angle -\theta_s$ and $I_s = (\pi/2)I_{bat}\angle -\theta_s$ (where $\theta_s \geq 0$), respectively, which provide correlated values when they are in phase at the fundamental frequency. The rectifier system's input impedance angle is denoted by θ_s. V_{bat} and I_{bat} represent the voltage and current levels of the battery, respectively. $R_L = V_s/I_s = (8/\pi^2)(V_{bat} + 2V_D)/I_{bat}$ can therefore be used to determine the load resistance as seen by the AC terminal of the rectifier. $2V_D$ accounts for the forward voltage drop in the rectifier circuit.

Once the input inverter's voltage in fundamental frequency and the passive elements in Figure 3.2 are obtained, first, the system without the EMO can be analyzed. The phasor currents can be described using the system's matrix model calculations, which are shown in equations (3.1) to (3.9). The angular switching frequency of the inverter is represented by the symbol ω_s in these formulas. The phasor currents of the transmitter and receiver coils, and induced eddy current in EMO are denoted by I_t, I_r, and I_E, respectively, in (3.1). By substituting the elements of each element in the matrix, it is evident that each diagonal element of the matrix is the complex numbers

with real and imaginary parts, due to them having their respective resistances of the coil, inverter and load.

$$\begin{bmatrix} V_t \\ \underbrace{V_{sx}}_{5\times1} \\ 0 \end{bmatrix} = \begin{bmatrix} Z_{t,t} & \underbrace{Z_{t,sx}}_{1\times5} & Z_{t,r} \\ \underbrace{Z_{sx,t}}_{5\times1} & \underbrace{Z_{sx,sx}}_{5\times5} & \underbrace{Z_{sx,r}}_{5\times1} \\ Z_{r,t} & \underbrace{Z_{r,sx}}_{1\times5} & Z_{r,r} \end{bmatrix} \begin{bmatrix} I_t \\ \underbrace{0}_{5\times1} \\ I_r \end{bmatrix} \tag{3.1}$$

$$\begin{bmatrix} \underbrace{I}_{7\times1} \end{bmatrix} = \begin{bmatrix} \underbrace{Z}_{7\times1} \end{bmatrix}^{-1} \begin{bmatrix} \underbrace{V}_{7\times1} \end{bmatrix} \tag{3.2}$$

$$Z_{t,t} = 2r_{DS} + R_t + \frac{1}{jw_sC_t} + jw_sL_t \tag{3.3}$$

$$Z_{t,sx} = \left[Z_{sx,t}\right]^T = \left[-jw_sM_{t,s1}, \dots, -jw_sM_{t,s5}\right] \tag{3.4}$$

$$Z_{t,r} = Z_{r,t} = -jw_sM_{t,r} \tag{3.5}$$

$$Z_{sx,sx}(i,i) = jw_sL_{si} + R_{si} \tag{3.6}$$

$$Z_{sx,sx}(i,j)|_{i\neq j} = Z_{sx,sx}(j,i)|_{i\neq j} = jw_sM_{si,sj} \tag{3.7}$$

$$Z_{sx,r} = \left[Z_{r,sx}\right]^T = \left[jw_sM_{s1,r}, \dots, jw_sM_{s5,r}\right]^T \tag{3.8}$$

$$Z_{r,r} = R_r + R_L + \frac{1}{jw_sC_r} + jw_sL_r \tag{3.9}$$

Next, using the system matrix without the presence of EMO, the equations for the sensing coil voltages V_{s1}, V_{s2}, V_{s3}, V_{s4}, V_{s5} and inverter current I_t is derived as follows:

$$V_{sx} = I_tZ_{sx,t} + 0 * Z_{sx,sx} + I_rZ_{sx,r} \tag{3.10}$$

$$0 = I_tZ_{r,t} + 0 * Z_{r,sx} + Z_{r,r}I_r \tag{3.11}$$

$$I_r = -I_t \frac{Z_{r,t}}{Z_{r,r}} \tag{3.12}$$

$$V_{sx} = I_t Z_{sx,t} - I_t \frac{Z_{r,t}}{Z_{r,r}} Z_{sx,r} \tag{3.13}$$

$$V_{sx} = I_t \left(\frac{Z_{sx,t} Z_{r,r} - Z_{r,t} Z_{sx,r}}{Z_{r,r}} \right) \tag{3.14}$$

$$V_{sx} = [V_{s1}, V_{s2}, V_{s3}, V_{s4}, V_{s5}]^T \tag{3.15}$$

Using linear combinations of every sense coil voltage, first, simplify the equations by introducing geometric parameter a_x, where *x* corresponds to each one of the open circuited sense coil voltages and then derive transmitter current I_t:

$$a_x = \frac{Z_{sx,t} Z_{r,r} - Z_{r,t} Z_{sx,r}}{Z_{r,r}} \tag{3.16}$$

$$a_x = [a_1, a_2, a_3, a_4, a_5] \tag{3.17}$$

$$I_t = \frac{1}{5} \sum_{i=1}^{5} V_{si} a_i = \frac{1}{5} (V_{s1} a_1 + V_{s2} a_2 + V_{s3} a_3 + V_{s4} a_4 + V_{s5} a_5) \tag{3.18}$$

As for the case of the presence of EMO in the operating area of the system, the matrix is going to expand with the addition of the induced eddy current on EMO, denoted by I_E:

$$\begin{bmatrix} V_t \\ \underbrace{V_{sx}}_{5\times1} \\ 0 \\ 0 \end{bmatrix} = \begin{bmatrix} Z_{t,t} & \underbrace{Z_{t,sx}}_{1\times5} & Z_{t,r} & Z_{t,E} \\ \underbrace{Z_{sx,t}}_{5\times1} & \underbrace{Z_{sx,sx}}_{5\times5} & \underbrace{Z_{sx,r}}_{5\times1} & \underbrace{Z_{sx,E}}_{5\times1} \\ Z_{r,t} & \underbrace{Z_{r,sx}}_{1\times5} & Z_{r,r} & Z_{r,E} \\ Z_{E,t} & \underbrace{Z_{E,sx}}_{1\times5} & Z_{E,r} & Z_{E,E} \end{bmatrix} \begin{bmatrix} I_t \\ \underbrace{0}_{5\times1} \\ I_r \\ I_E \end{bmatrix} \tag{3.19}$$

$$\begin{bmatrix} \underbrace{I}_{8\times1} \end{bmatrix} = \begin{bmatrix} \underbrace{Z}_{8\times1} \end{bmatrix}^{-1} \begin{bmatrix} \underbrace{V}_{8\times1} \end{bmatrix} \tag{3.20}$$

$$Z_{t,t} = 2r_{DS} + R_t + \frac{1}{jw_s C_t} + jw_s L_t \tag{3.21}$$

$$Z_{t,sx} = \left[Z_{sx,t}\right]^T = \left[-jw_s M_{t,s1}, \dots, -jw_s M_{t,s5}\right] \tag{3.22}$$

$$Z_{t,r} = Z_{r,t} = -jw_s M_{t,r} \tag{3.23}$$

$$Z_{t,E} = Z_{E,t} = -jw_s M_{t,E} \tag{3.24}$$

$$Z_{sx,sx}(i,i) = jw_s L_{si} + R_{si} \tag{3.25}$$

$$Z_{sx,sx}(i,j)|_{i\neq j} = Z_{sx,sx}(j,i)|_{i\neq j} = jw_s M_{si,sj} \tag{3.26}$$

$$Z_{sx,r} = \left[Z_{r,sx}\right]^T = \left[jw_s M_{s1,r}, \dots, jw_s M_{s5,r}\right]^T \tag{3.27}$$

$$Z_{sx,E} = \left[Z_{E,sx}\right]^T = \left[jw_s M_{s1,E}, \dots, jw_s M_{s5,E}\right]^T \tag{3.28}$$

$$Z_{r,r} = R_r + R_L + \frac{1}{jw_s C_r} + jw_s L_r \tag{3.29}$$

$$Z_{r,E} = Z_{E,r} = jw_s M_{r,E} \tag{3.30}$$

$$Z_{E,E} = R_E + jw_s L_E \tag{3.31}$$

The objective is to analyze and derive the equations for the transmitter current and sensing coil voltages with the presence of the EMO to observe the changes it causes. It can be done by applying matrix reduction method, where I_E is going to be expressed in terms of I_t and I_r.

$$I_E = -\frac{Z_{E,t} I_t + Z_{E,sx} * 0 + Z_{E,r} I_r}{Z_{E,E}} \tag{3.32}$$

$$\begin{bmatrix} V_t \\ \underbrace{V_{sx}}_{5\times1} \\ 0 \end{bmatrix} = \begin{bmatrix} Z'_{t,t} & \underbrace{Z'_{t,sx}}_{1\times5} & Z'_{t,r} \\ \underbrace{Z'_{sx,t}}_{5\times1} & \underbrace{Z'_{sx,sx}}_{5\times5} & \underbrace{Z'_{sx,r}}_{5\times1} \\ Z'_{r,t} & \underbrace{Z'_{r,sx}}_{1\times5} & Z'_{r,r} \end{bmatrix} \begin{bmatrix} I'_t \\ \underbrace{0}_{5\times1} \\ I'_r \end{bmatrix} \tag{3.33}$$

$$Z'_{t,t} = Z_{t,t} - \frac{Z_{t,E}Z_{E,t}}{Z_{E,E}} \tag{3.34}$$

$$Z'_{t,sx} = \left[Z'_{sx,t}\right]^T = Z_{t,sx} - \frac{Z_{t,E}Z_{E,sx}}{Z_{E,E}} \tag{3.35}$$

$$Z'_{t,r} = Z'_{r,t} = Z_{t,r} - \frac{Z_{t,E}Z_{E,r}}{Z_{E,E}} \tag{3.36}$$

$$Z'_{sx,sx} = Z_{sx,sx} - \frac{Z_{sx,E}Z_{E,sx}}{Z_{E,E}} \tag{3.37}$$

$$Z'_{sx,r} = \left[Z'_{r,sx}\right]^T = Z_{sx,r} - \frac{Z_{sx,E}Z_{E,r}}{Z_{E,E}} \tag{3.38}$$

$$Z'_{r,r} = Z_{r,r} - \frac{Z_{r,E}Z_{E,r}}{Z_{E,E}} \tag{3.39}$$

$$Z'_{t,t} = 2r_{DS} + R_t + \frac{1}{jw_sC_t} + jw_sL_t + \frac{w_s^2M_{t,E}^2}{R_E + jw_sL_E}$$

$$= 2r_{DS} + R_t + \underbrace{\frac{w_s^2M_{t,E}^2R_E}{R_E^2 + w_s^2L_E^2}}_{\substack{Added\ self \\ resistance}} + \frac{1}{jw_sC_t} + jw_s\left(L_t - \underbrace{\frac{w_s^2M_{t,E}^2L_E}{R_E^2 + w_s^2L_E^2}}_{\substack{Substracted\ self \\ inductance}}\right) \tag{3.40}$$

$$Z'_{t,sx} = \left[Z'_{t,sx}\right]^T = -jw_sM_{t,sx} + \frac{w_s^2M_{sx,E}M_{t,E}}{R_E + jw_sL_E}$$

$$= \underbrace{\frac{w_s^2M_{sx,E}M_{t,E}R_E}{R_E^2 + w_s^2L_E^2}}_{\substack{Introduced\ mutual \\ resistance}} - jw_s\left(M_{t,sx} - \underbrace{\frac{w_s^2M_{sx,E}M_{t,E}L_E}{R_E^2 + w_s^2L_E^2}}_{\substack{Substracted\ imaginary \\ term}}\right) \tag{3.41}$$

$$Z'_{r,sx} = \left[Z'_{sx,r}\right]^T = jw_s M_{r,sx} - \frac{w_s^2 M_{sx,E} M_{r,E}}{R_E + jw_s L_E}$$

$$= -\underbrace{\frac{w_s^2 M_{sx,E} M_{r,E} R_E}{R_E^2 + w_s^2 L_E^2}}_{\substack{Introduced\ mutual \\ resistance}} + jw_s \left(M_{r,sx} + \underbrace{\frac{w_s^2 M_{sx,E} M_{r,E} L_E}{R_E^2 + w_s^2 L_E^2}}_{\substack{Added\ imaginary \\ term}} \right) \tag{3.42}$$

$$Z'_{r,r} = R_r + R_L + \frac{1}{jw_s C_r} + jw_s L_r + \frac{w_s^2 M_{r,E}^2}{R_E + jw_s L_E}$$

$$= R_r + R_L + \underbrace{\frac{w_s^2 M_{r,E}^2 R_E}{R_E^2 + w_s^2 L_E^2}}_{\substack{Added\ self \\ resistance}} + \frac{1}{jw_s C_r} + jw_s \left(L_r - \underbrace{\frac{w_s^2 M_{r,E}^2 L_E}{R_E^2 + w_s^2 L_E^2}}_{\substack{Substracted\ self \\ inductance}} \right) \tag{3.43}$$

$$Z'_{t,r} = Z'_{r,t} = -jw_s M_{t,r} - \frac{w_s^2 M_{t,E} M_{r,E}}{R_E + jw_s L_E}$$

$$= -\underbrace{\frac{w_s^2 M_{t,E} M_{r,E} R_E}{R_E^2 + w_s^2 L_E^2}}_{\substack{Introduced\ mutual \\ resistance}} - jw_s \left(M_{t,r} + \underbrace{\frac{w_s^2 M_{t,E} M_{r,E} L_E}{R_E^2 + w_s^2 L_E^2}}_{\substack{Added\ imaginary \\ term}} \right) \tag{3.44}$$

As a result of the performed analysis, by comparing the derived expressions of (3.41), (3.42), (3.43) and (3.44) with (3.4), (3.8), (3.9), and (3.5) respectively, it is evident that the proximity effect and the presence of EMO brings in mutual resistance between transmitter and each of sensing coils, transmitter and receiver, and transmitter and receiver and each of sensing coils. As for the cases of transmitter and receiver coils, mentioned effects increment the self-resistances and decrement the values of self-inductances. Those changes in the equations were the outcome of the self and mutual properties of the eddy currents and affect all the parameters of the reduced impedance matrix. To examine to what extent it affected the system, 3-D FEA is performed in the following section.

Apply the same analysis performed for the system matrix of the system without EMO by deriving the equations for the sensing coil voltages V_{s1}, V_{s2}, V_{s3}, V_{s4}, V_{s5} and inverter current I_t:

$$V_{sx} = I_t' Z_{sx,t}' + 0 * Z_{sx,sx}' + I_r' Z_{sx,r}' \tag{3.45}$$

$$0 = I_t' Z_{r,t}' + 0 * Z_{r,sx}' + Z_{r,r}' I_r' \tag{3.46}$$

$$I_r' = -I_t' \frac{Z_{r,t}'}{Z_{r,r}'} \tag{3.47}$$

$$V_{sx} = I_t' Z_{sx,t}' - I_t' \frac{Z_{r,t}'}{Z_{r,r}'} Z_{sx,r}' \tag{3.48}$$

$$V_{sx} = I_t' \left(\frac{Z_{sx,t}' Z_{r,r}' + Z_{r,t}' Z_{sx,r}'}{Z_{r,r}'} \right) \tag{3.49}$$

$$V_{sx} = [V_{s1}, V_{s2}, V_{s3}, V_{s4}, V_{s5}]^T \tag{3.50}$$

Using linear combinations of every sense coil voltage, first, simplify the equations by introducing adverse geometric parameter a_x', where *x* corresponds to each one of the open circuited sense coil voltages and then derive transmitter current I_t' with the presence of EMO:

$$a_x' = \frac{Z_{sx,t}' Z_{r,r}' + Z_{r,t}' Z_{sx,r}'}{Z_{r,r}'} \tag{3.51}$$

$$a_x' = [a_1, a_2, a_3, a_4, a_5] \tag{3.52}$$

$$I_t' = \frac{1}{5} \sum_{i=1}^{5} V_{si} a_i' = \frac{1}{5} (V_{s1} a_1' + V_{s2} a_2' + V_{s3} a_3' + V_{s4} a_4' + V_{s5} a_5') \tag{3.53}$$

It is apparent that, the magnetic couplings relation between the transmitter, receiver and sensing coils are contained in geometric parameters, which are first calibrated in the base model and then recorded. Following calibration, transmitter coil current and sensing coil voltage readings are used. By employing the first calibrated geometric parameters, the transmitter coil current is

reconstructed from a linear combination of the sensing coil voltages. An external object in the electromagnetic space creates a sequent error from the increased coupling between the foreign object and other coils. EOs are recognized from the sequent error between the measured and reconstructed transmitter coil current.

Sequent error can be denoted as ϵ_D, where the percentage error depends on the geometric parameters α_1 and α_2, can be written as follows:

$$\epsilon_D = \left|\frac{I_T - I_t}{I_T}\right| * 100(\%) \tag{3.54}$$

where I_t refers to the calibrated transmitter current by sense voltages and I_T is the transmitter current readings from the current sensor.

3.3 Finite Element Analysis on the Effects of EMO on the WPT-EOD System

Proposed WPT-EOD system undergoes a thorough 3-D eddy current FEA. There are four scenarios for the conducted simulations that are present in the Figure 3.3. In the first case scenario the simulation is conducted without any EMO and for the other three cases, EMO were chosen as such, so that their dimensions were varied from each other. In the simulation environment, the transmitter and receiver coils are excited with a 5 A simultaneously in the frequency range from 10 kHz to 1 MHz and from 80 kHz to 90 kHz.

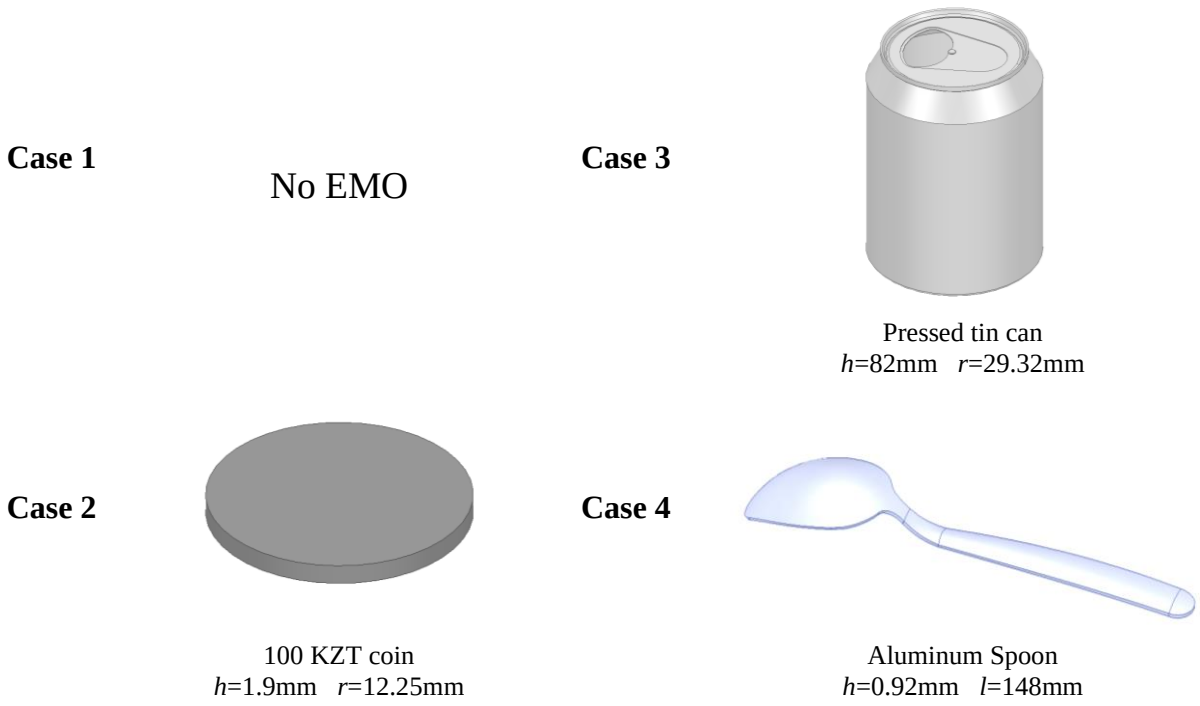

Figure 3.3: Four simulation cases in Ansys Electronics Desktop

For the simulation purposes, transmitter and receiver coils have the same base geometry with a space turn of 2 mm, an inner radius of 100 mm, a strand number of 100, and a turn number of 20. Considering the taken geometry of the coils, outer radius of both coils equals to about 200 mm. The distance between transmitter and receiver coils is chosen to be 15 cm because it suits the ground clearance of the EVs in the industry such as Nissan Leaf [39]. Regarding single-turn open-circuited sensing coils, they were placed above the transmitter coil in the height of 2 cm. Each EMOs are placed 4 cm above transmitter coil. The first sensing coil has a radius of 200 mm and each subsequent coils have a radius reduced by 10 mm from the previously placed sensing coil. The example of the simulation setup with the presence of EMO is illustrated in Figure 3.4:

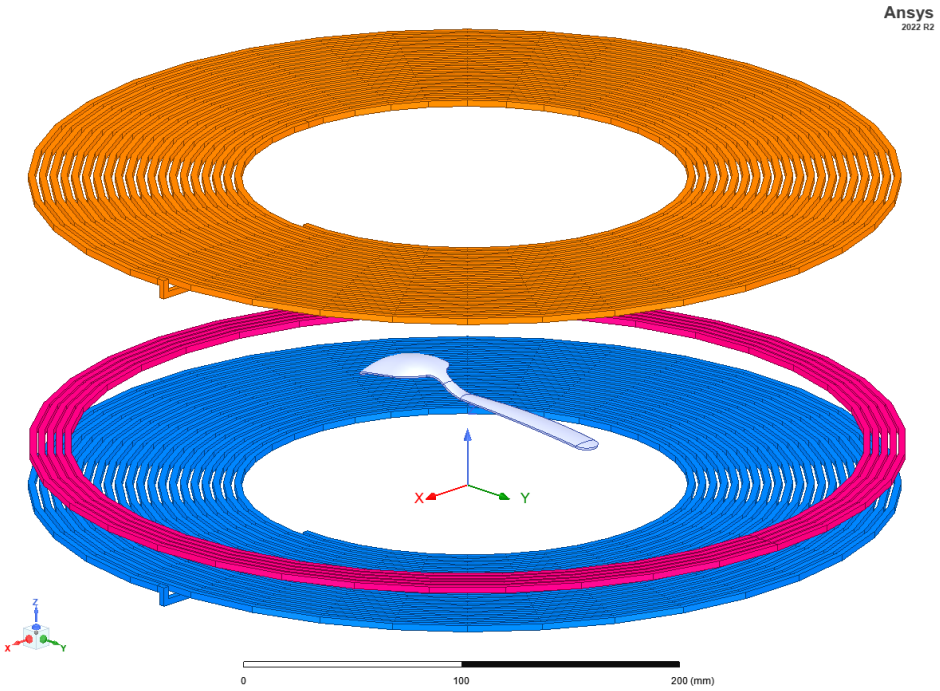

Figure 3.4: Simulation setup of the case 4 in the Ansys Electronics Desktop

The acquired data from the ANSYS Electronics Desktop for the case of no EMO of the sense coil voltages and, self-inductances and resistances for the wide range of frequencies from 10 kHz to 1 MHz, where each case were differentiated by 50 kHz and its visualization can be seen in Figure 3.5 and Figure 3.6:

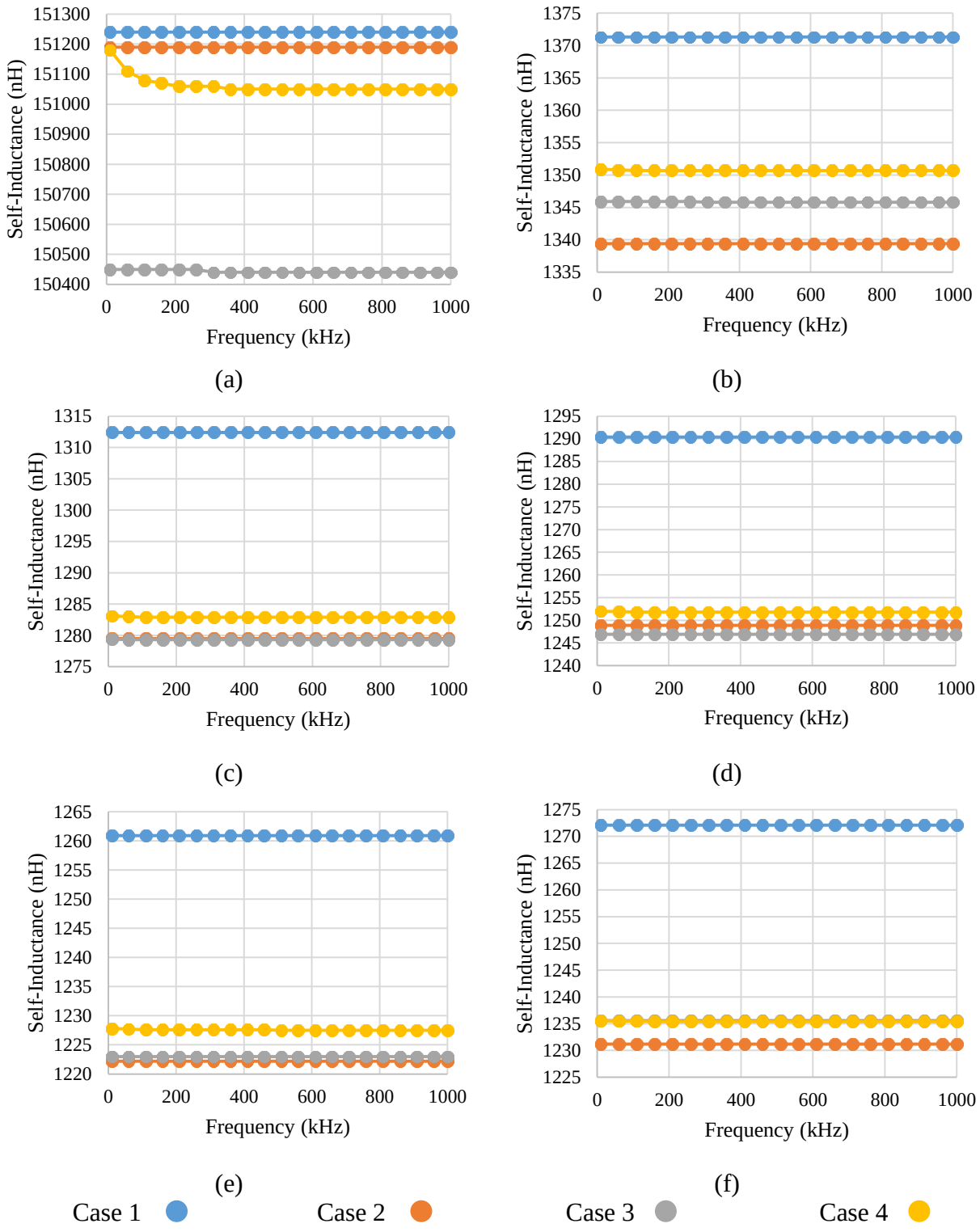

Figure 3.5: Self-inductance of (a) Transmitter coil, (b) S1 coil, (c) S2 coil, (d) S3 coil, (e) S4 coil, and (f) S5 coil over the range of frequency from 10 kHz to 1 MHz

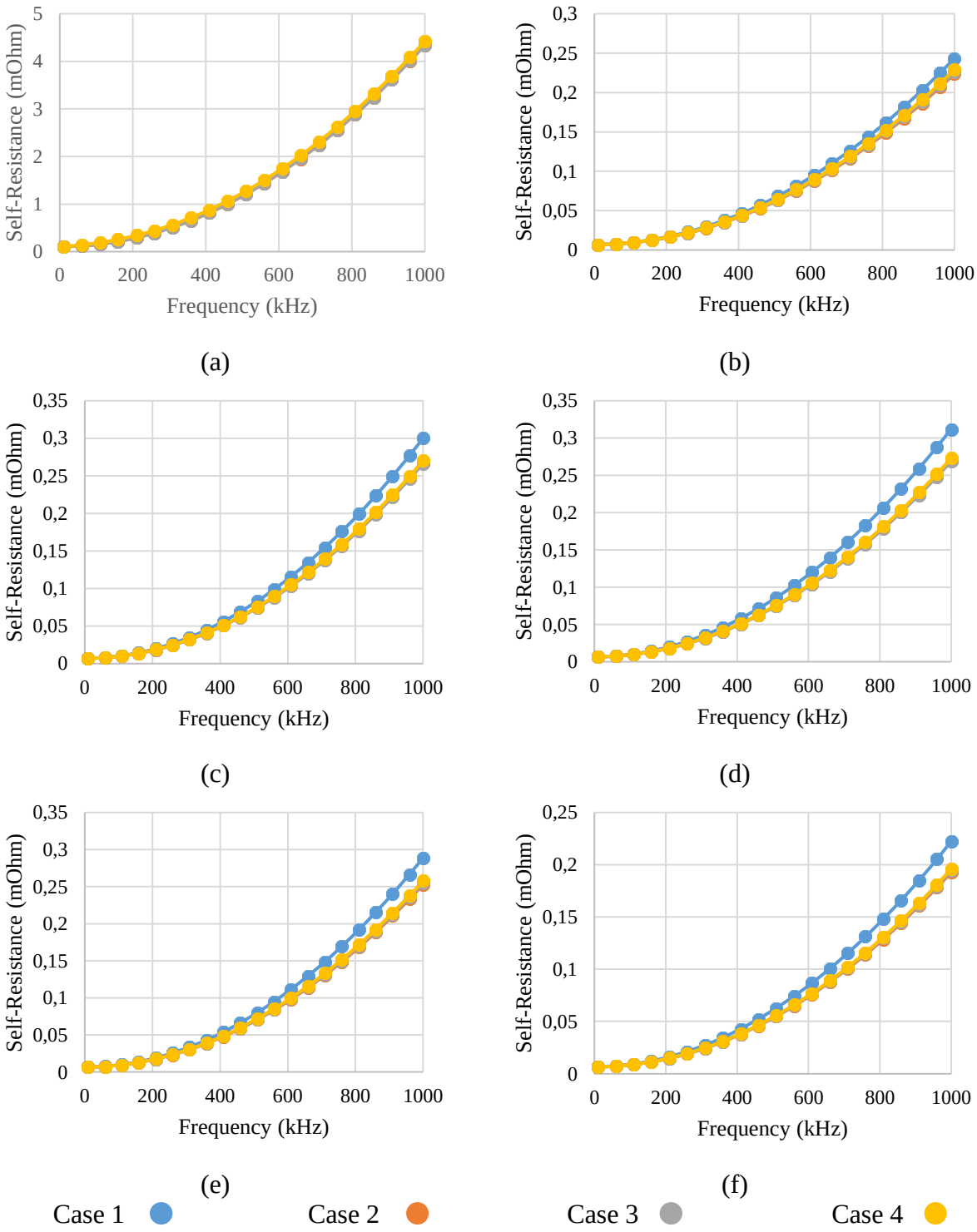

Figure 3.6: Self-resistance of (a) Transmitter coil, (b) S1 coil, (c) S2 coil, (d) S3 coil, (e) S4 coil, and (f) S5 coil over the range of frequency from 10 kHz to 1 MHz

As for the frequency range from 80 kHz to 90 kHz, the results for the self-inductance and resistance are present below in the Figure 3.7 and Figure 3.8:

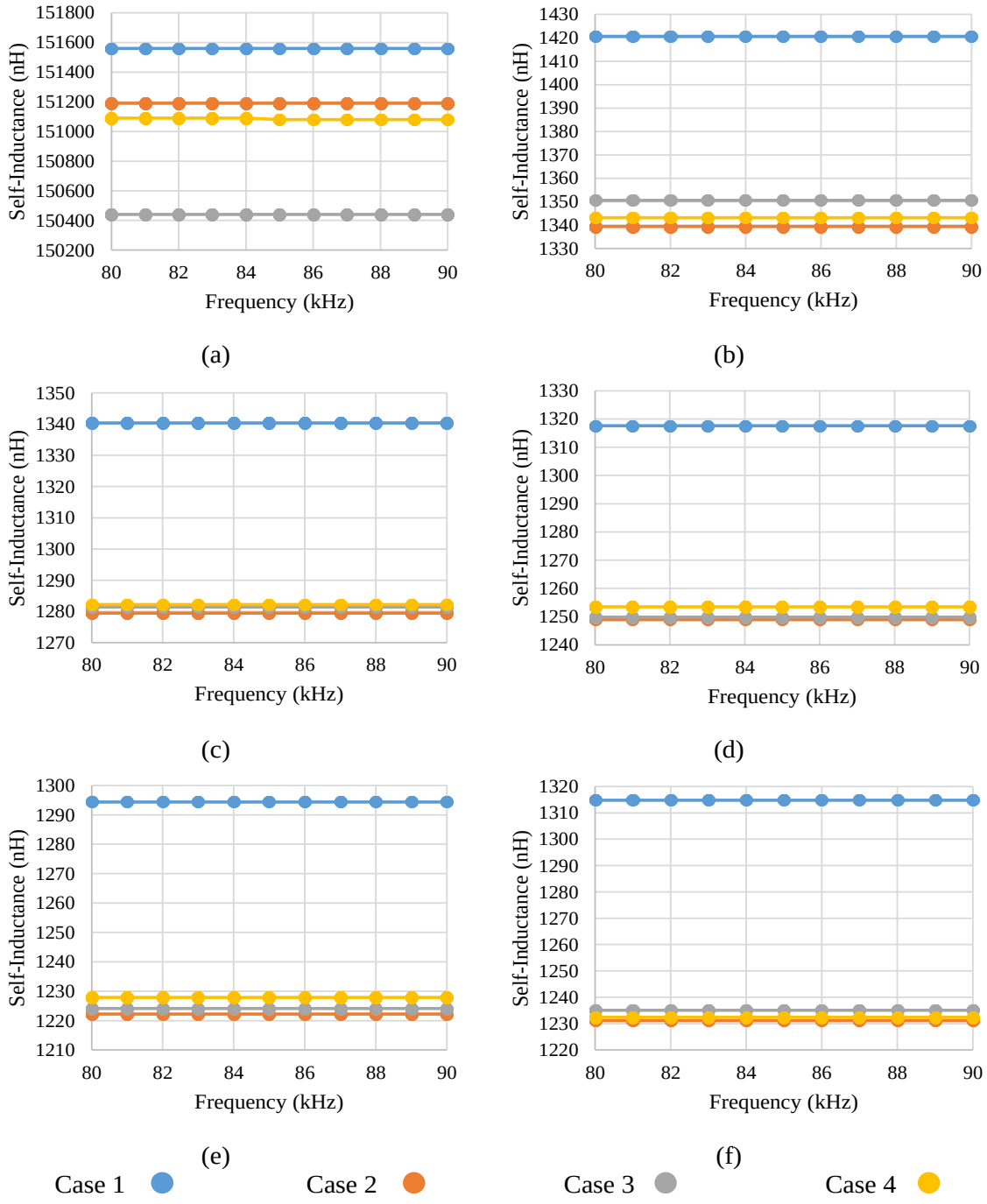

Figure 3.7: Self-inductance of (a) Transmitter coil, (b) S1 coil, (c) S2 coil, (d) S3 coil, (e) S4 coil, and (f) S5 coil over the range of frequency from 80 kHz to 90 kHz

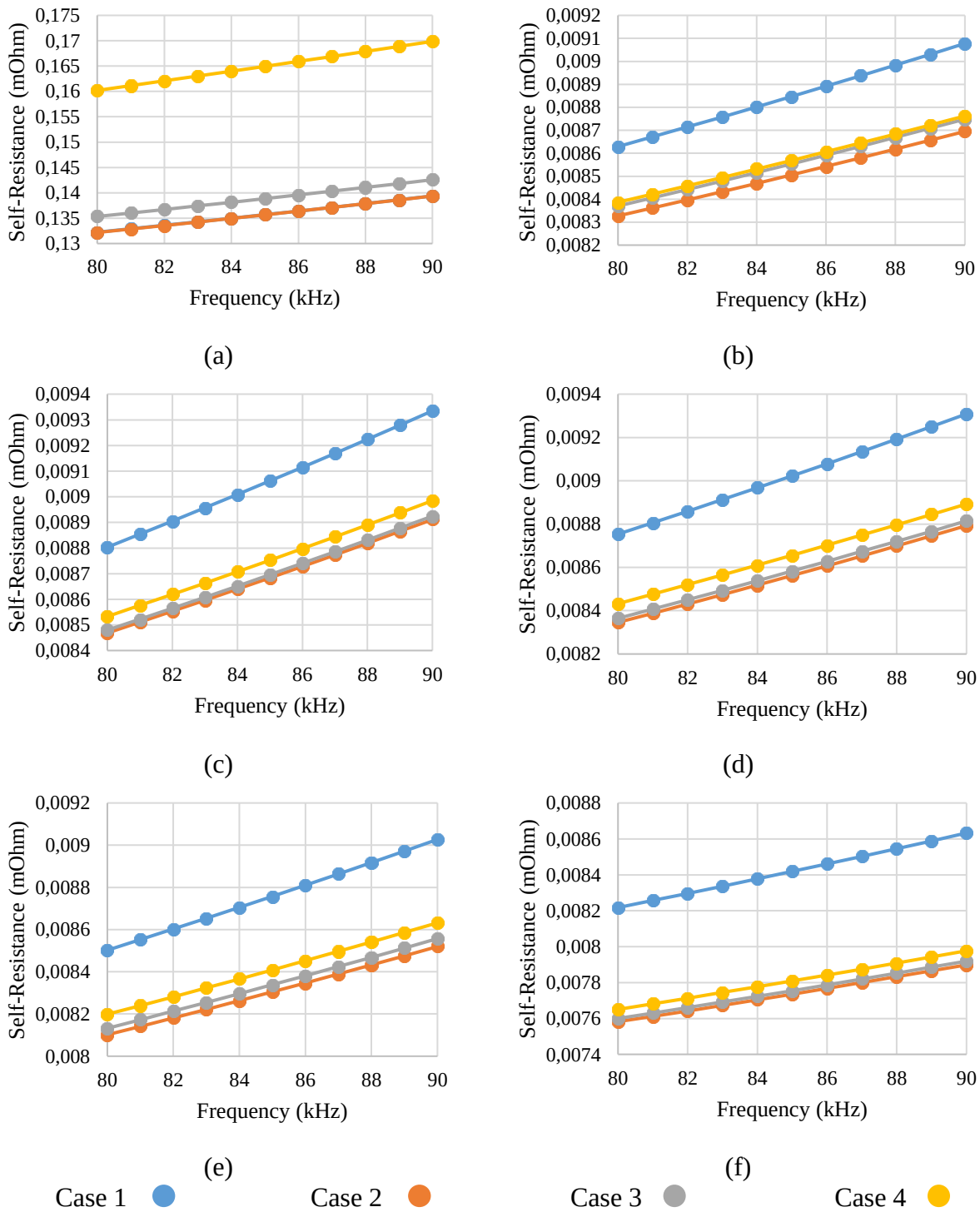

Figure 3.8: Self-resistance of (a) Transmitter coil, (b) S1 coil, (c) S2 coil, (d) S3 coil, (e) S4 coil, and (f) S5 coil over the range of frequency from 80 kHz to 90 kHz

Looking at the results of collecting data from the FEA technique, it can be seen that over the wide range of self-inductance of each coils stays the same, which shows that the self-inductance parameter of the coil itself is not dependent of the frequency at which the system operates, which is also shown in equation below:

$$L = \frac{N^2(D_i + N(D_w + s) - s)^2}{60(D_i + N(D_w + s) - s) - 44D_i} \tag{3.55}$$

This is Wheeler's high-accurate formula for computing self-inductance of a core-less flat spiral coils [40].

Another conclusion that we can make is that self-resistance parameter of the transmitter coil becomes higher in the presence of the EMO and it stays that way across the range of frequencies, whereas the sensing coils' self-resistance parameter becomes smaller in the presence of EMO with the very small change at the lower frequencies and higher change at the highest frequencies.

Regarding the proposed methods ability of EOD across the range of frequencies. As the proposed method suggests, in order to obtain the geometric parameters a_i, they need to be calibrated in the base model of the system where no EMO is present. Using FEA technique, the data of the induced voltages in sense coils were collected across the wide range of frequencies. From the collected data across frequencies, which is labeled as *n*, the matrix for the voltage, a data vector for the current in transmitter coil, and a data vector for the geometric parameters are created:

$$V = \begin{bmatrix} V_1(f_1) & \cdots & V_5(f_1) \\ \vdots & \ddots & \vdots \\ V_1(f_n) & \cdots & V_5(f_n) \end{bmatrix} \tag{3.56}$$

$$I_T = [I_T(f_1) \dots I_T(f_n)]^T \tag{3.57}$$

$$a = [a_1\ a_2\ a_3\ a_4\ a_5]^T \tag{3.58}$$

After the parameters were established, the geometric parameters can be found using the method of least-squares:

$$a = (V^T V)^{-1} V^T I_T \tag{3.59}$$

For the case of wide range of frequency, which is from 10 kHz to 1 MHz, the geometric parameters were calibrated using five sensing coil voltage and transmitter current readings across frequency spectrum (3.59), and EOD is performed using equation (3.54) in Figure 3.9:

$$a = [4.068754, 107.1975, 101.1746, -45.8134, -162.794]$$

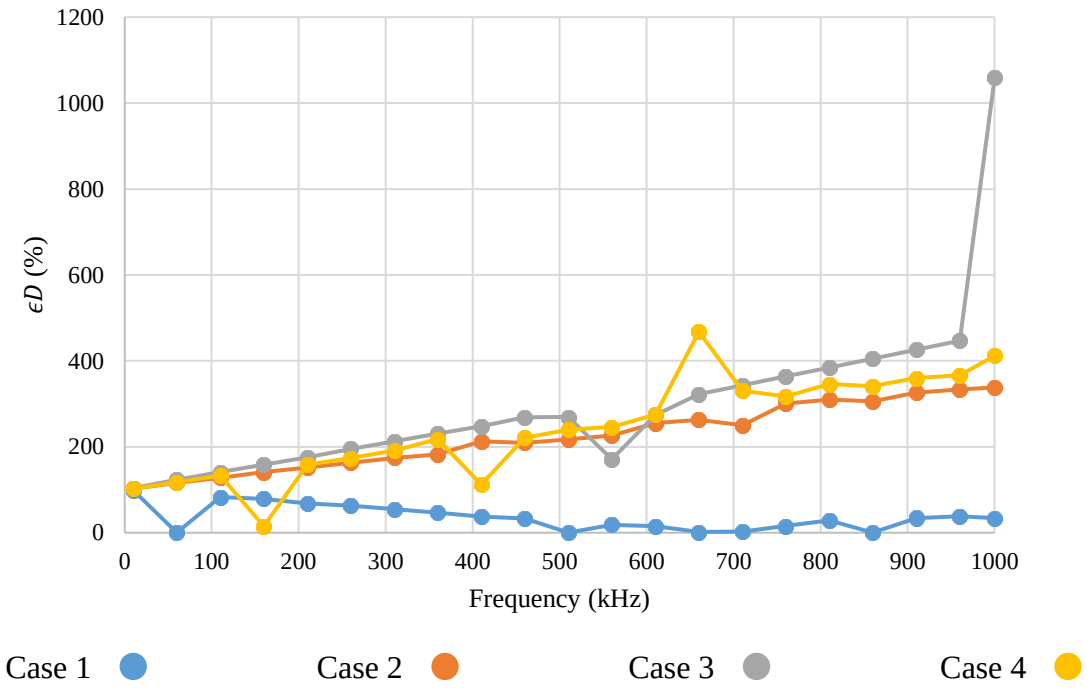

Figure 3.9: Sequent error results of the four simulation cases over the range of frequency from 10 kHz to 1 MHz

And for the case of ranging frequency from 80 kHz to 90 kHz, using the same approach the geometric parameters were calibrated and obtained values are as follows:

$$a = [419.2887, -492, 164.4657, 39.59464, -124.874]$$

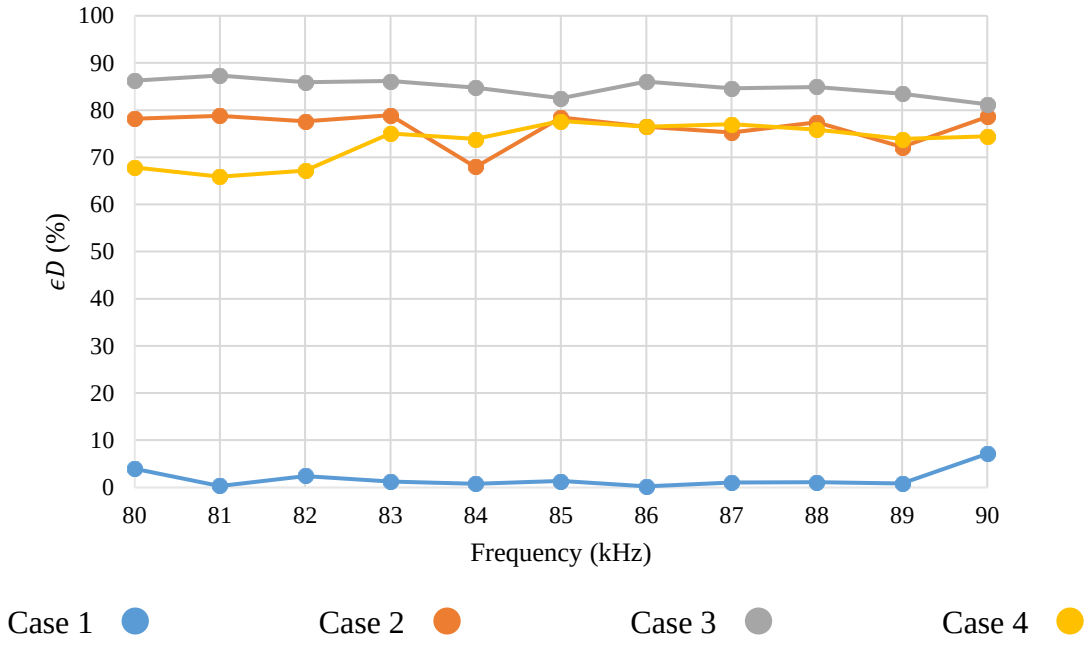

Figure 3.10: Sequent error results of the four simulation cases over the range of frequency from 80 kHz to 90 kHz

By comparing two cases of varying frequency, as it can be observed from Figure 3.9, the large range of frequency the proposed detection strategy falls apart and becomes unreliable, whereas in the case of smaller in comparison frequency range such as shown in Figure 3.10, the results show clear distinction between the Case 1, which is without the presence of EMO and the other three case, where EMO takes part in the system. This can be explained by the Faraday's Law of Electromagnetic Induction, where the induced voltage of a coil is magnetic flux dependent,

where in turn magnetic flux is magnetic field dependent by making the induced voltage value proportional to the operating frequency of the transmitter side of the system [41]:

$$V = -N\frac{d\Phi}{dt} \tag{3.60}$$

$$\Phi = \mathrm{B} * \mathrm{S} * \cos(\theta) \tag{3.61}$$

That is the reason, as the operating frequency increases, the induced voltage values increase too, leading to a large value difference between the induced voltage values at 10 kHz and 1 MHz, which in turn makes it hard to derive geometric parameters that will work across the large range of frequency.

Chapter 4 – Experimental Setup

4.1 Information on the setup

The experimental setup for the proposed system is shown in Figure 4.1. The setup consists of 1) EL302RT Triple Power Supply device which serves a purpose of energizing the inverter with 12V and to be an input power source for the system; 2) Full-Bridge Inverter that transforms DC to AC; 3) Main setup that consists of transmitter, receiver and five open-circuited sensing coils; 4) Full-bridge rectifier circuit that transforms induced AC voltage and current in the receiver coil into DC; 5) BK PREDCISION 8600 DC Electronic Load modifying which system's imaginary load is created; 6) HDO8108R 1 GHz High Definition Oscilloscope is used to measure data from the sensing coil voltages and transmitter currents.

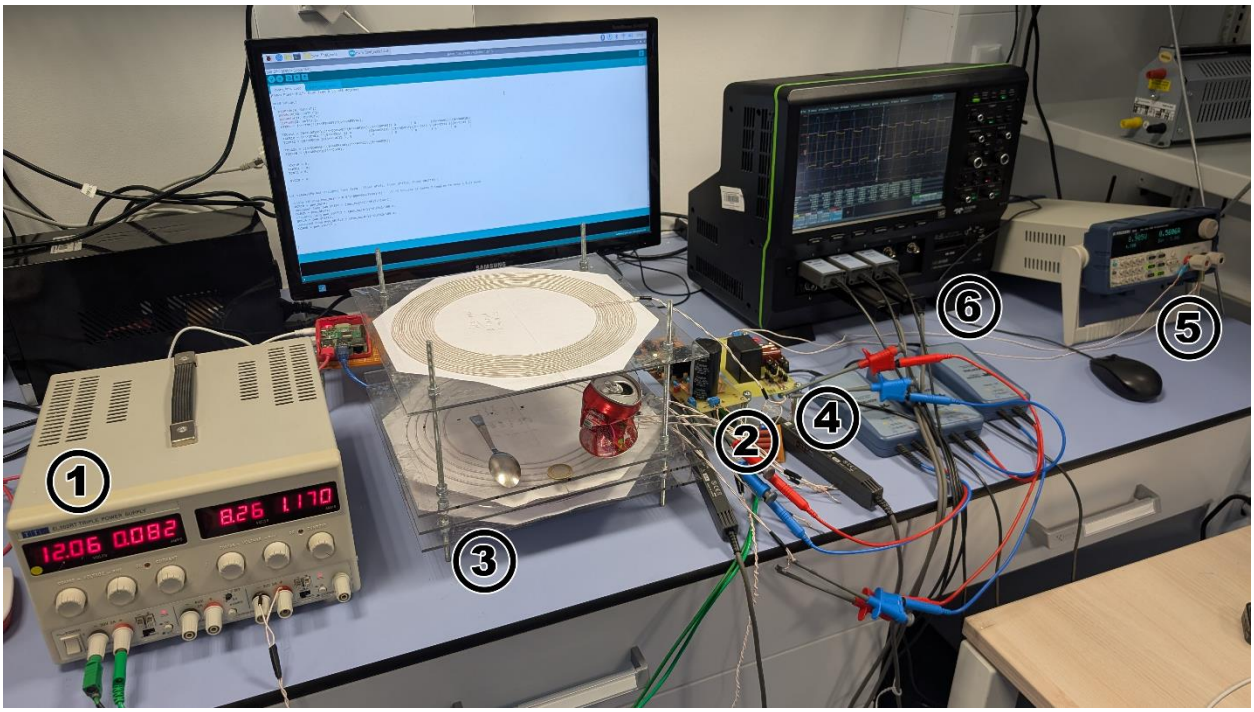

Figure 4.1: The experimental setup of the proposed system: 1) power supply; 2) inverter; 3) coil setup; 4) rectifier; 5) electronic load; 6) oscilloscope.

The assembled experimental setup undergoes four testing cases similarly to the ones that were carried out in the previous sections:

Case 1

No EMO

Case 3

Pressed tin can
h=8mm *r*31mm

Case 2

1 TRY coin
h=1.9mm *r*=13mm

Case 4

Aluminum Spoon
h=1.5mm *l*=144mm

Figure 4.2: Four experimental cases for the experimental setup

The close-up of the main setup is shown in Figure 4.3. As it can be seen, main setup consists of four layers, where transmitter coil is set at the bottom first layer, five open-circuited sensing coils are located above first layer, creating the second layer, third layer which is made for the EMOs to be placed at, and the last top layer is the receiver coil.

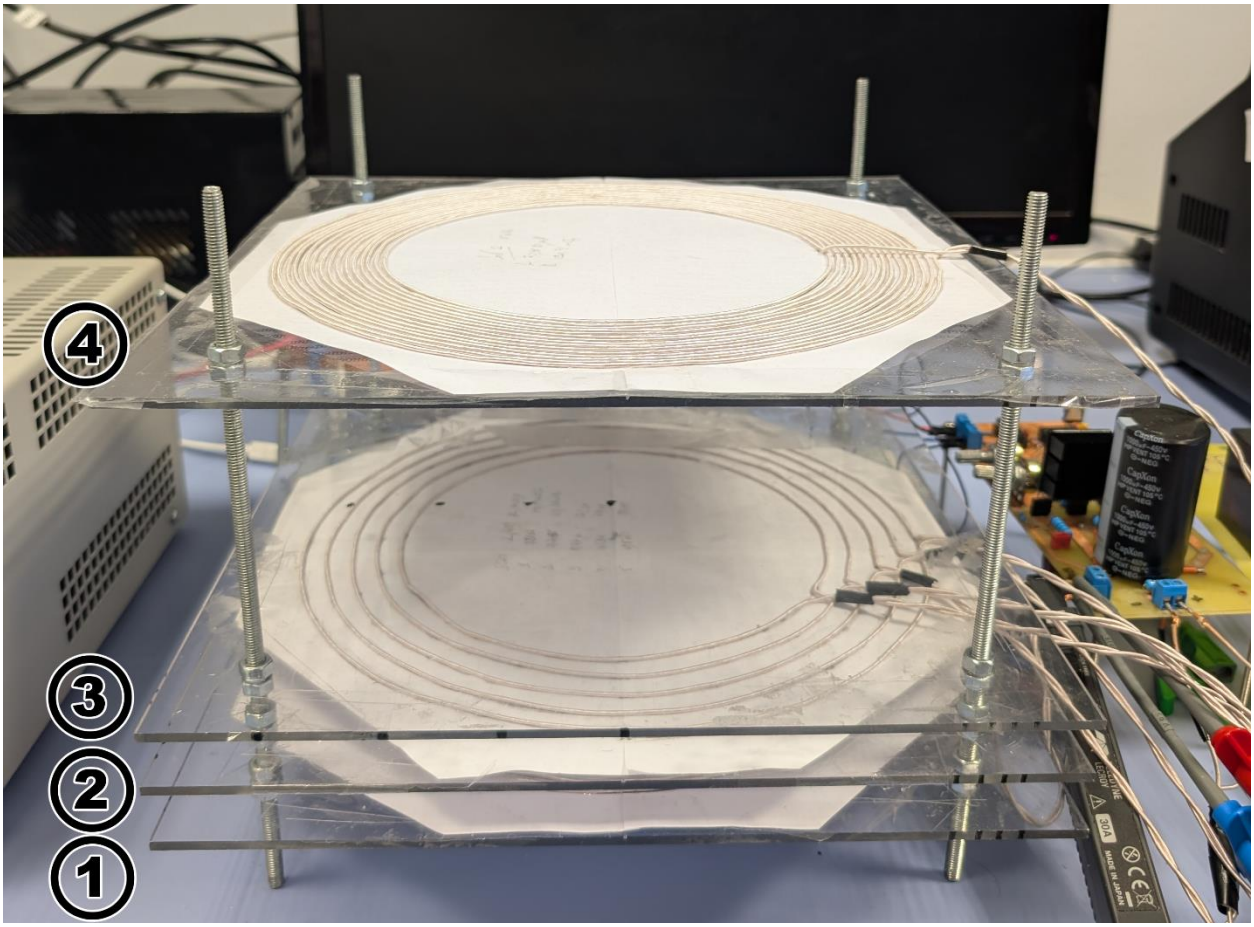

Figure 4.3: Coil setup of the proposed EOD method: 1) transmitter coil; 2) five open-circuited sensing coils; 3) space for EMO; 4) receiver coil.

Transmitter and receiver coils were made with the outer radius being 13 cm, inner radius being 9 cm, number of turns being 15, strand number being 160 and wire diameter being 1 mm, and with space between wires being 0.4 cm. The radius of the sensing coils starts from 13 cm and decreases by the 1 cm with next sensing coil, which is in our case are 12 cm, 11 cm, 10 cm, and 9 cm.

4.2 Measurement of Coil Parameters

One of the main goals of this experimental setup is to measure self-inductances and self-resistances of the transmitter and sensing coils in four cases in the frequency spectrum from 80 kHz to 90 kHz:

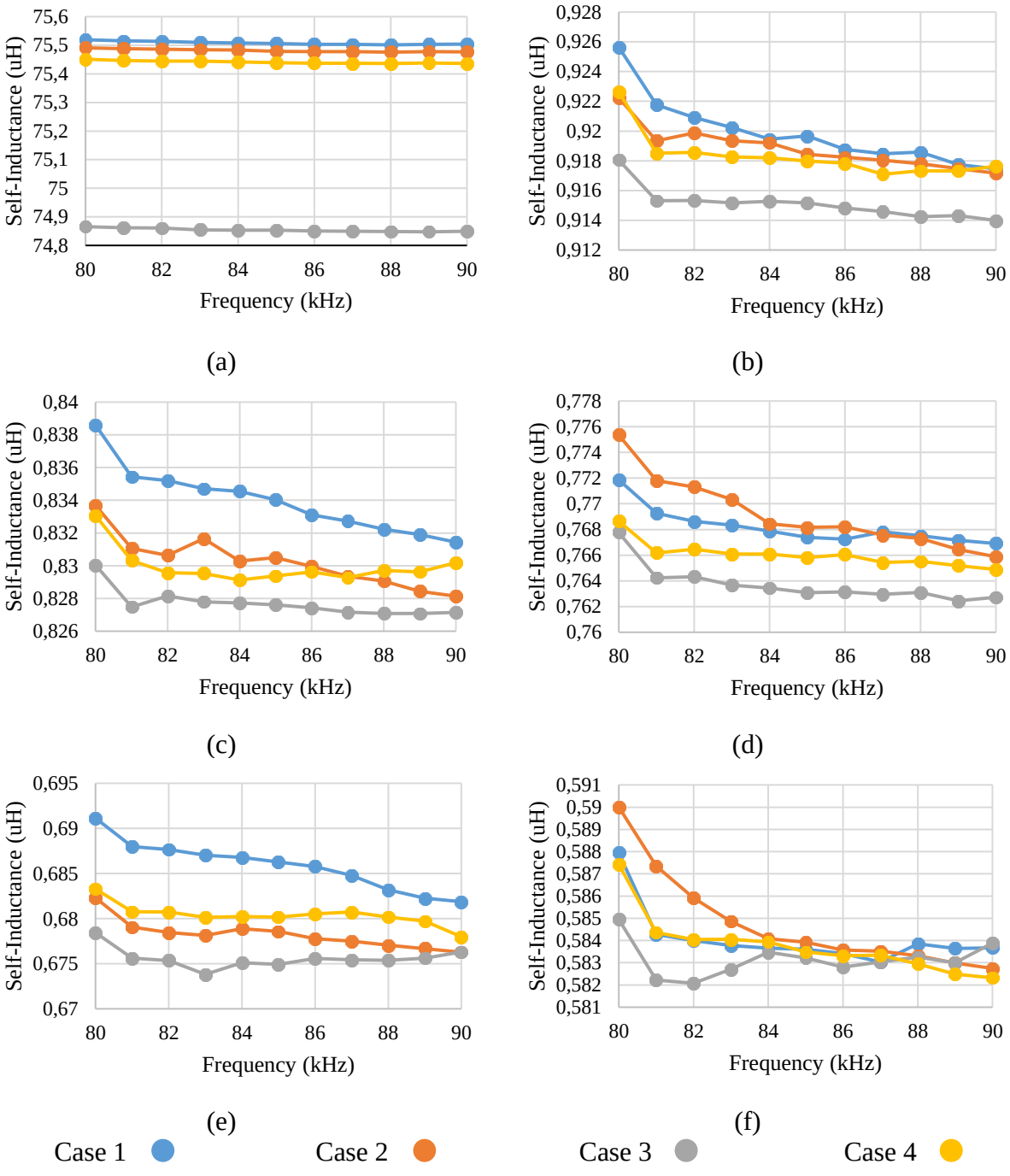

Figure 4.4: Measurement of self-inductance of (a) Transmitter coil, (b) S1 coil, (c) S2 coil, (d) S3 coil, (e) S4 coil, and (f) S5 coil over the range of frequency from 80 kHz to 90 kHz

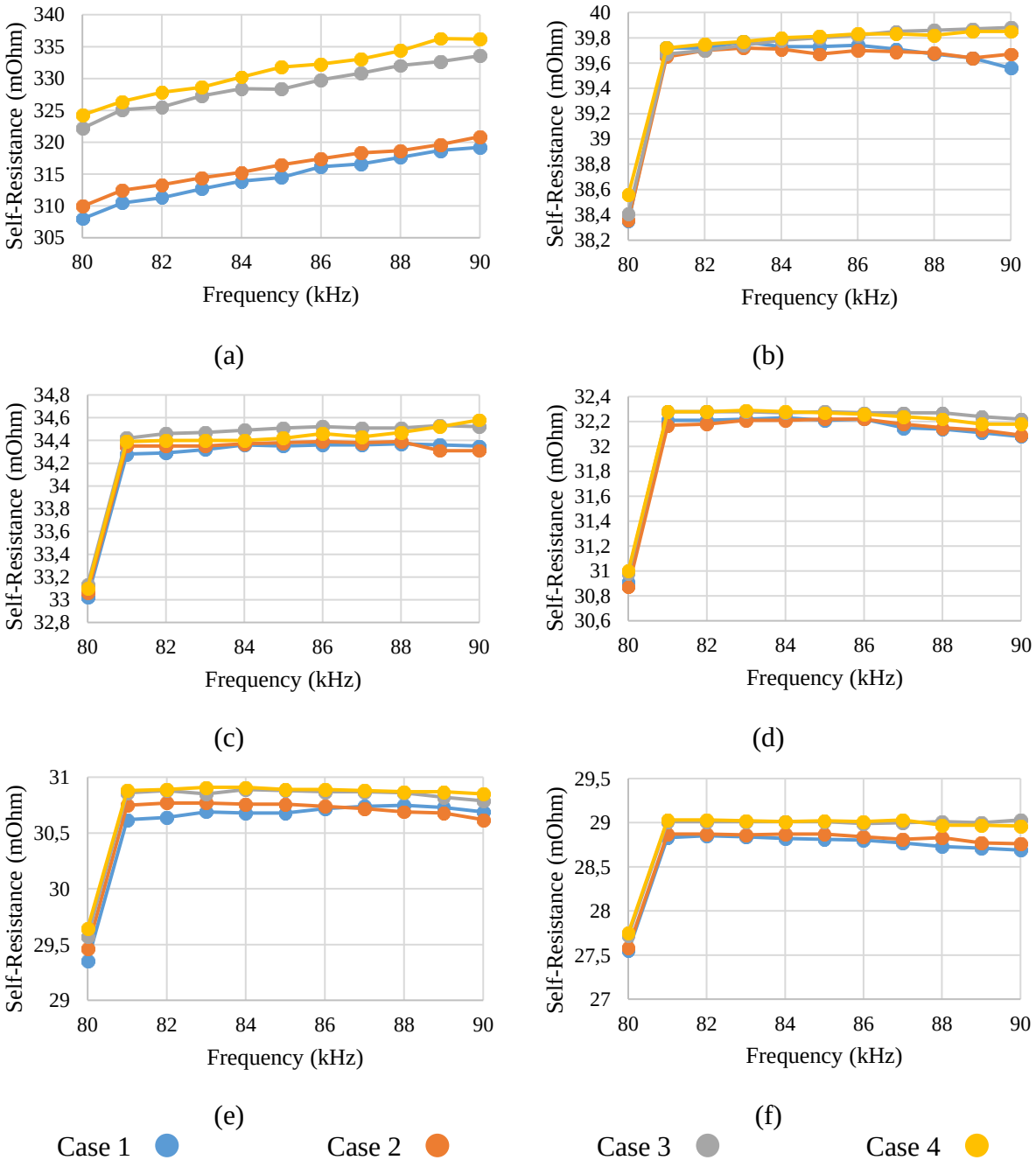

Figure 4.5: Measurement of self-resistance of (a) Transmitter coil, (b) S1 coil, (c) S2 coil, (d) S3 coil, (e) S4 coil, and (f) S5 coil over the range of frequency from 80 kHz to 90 kHz

As a result, without EMO, no frequency dependency is explored as previously stated by the Wheeler's formula (3.55). It is also proven in the sensing coils as well but with small deviations occurred due to eddy current-induced changes. In the case of self-resistance values, they increase as the frequency becomes higher due to skin effect even with the use of Litz wires. Additionally, it can be seen that in the presence of EMO the value is tend to increase. Case 4, which is the case of Aluminum spoon also shows higher increment in self-resistance that the other EMO cases due to it covering larger surface area, whereas the higher impact on the self-inductances is caused by the tin can.

4.3 MOD at Constant Current and Constant Input Power Cases

The next experimental procedure is to perform MOD over the frequency spectrum from 80 kHz to 90 kHz. In the case of experimental setup, due to technical reasons, it is unable to perform WPT over the spectrum of frequencies by managing to simultaneously maintain transmitter current of 2 A and input power level at 10 W. Due to this reason, it was decided to perform two experimental procedures with maintaining transmitter current of 2 A and in the other procedure to maintain input power at 10 W over the span of frequencies from 83.3 kHz to 86.9 kHz. The reasons for this specific frequency range also lies in the technical reasons, where PWM signal, which is generated using Arduino Uno is able to produce only specific values of frequencies, such as 83.3 kHz, 84.1 kHz, 85 kHz, 85.9 kHz and 86.8 kHz.

In the first experimental procedure, where the 2 A of transmitter current is maintained across frequencies the obtained geometric parameters and the sequent error results are as follows:

$$a = [-5.232483625, -0.497182242, -2.097068643, 8.366829842, 1.352582627]$$

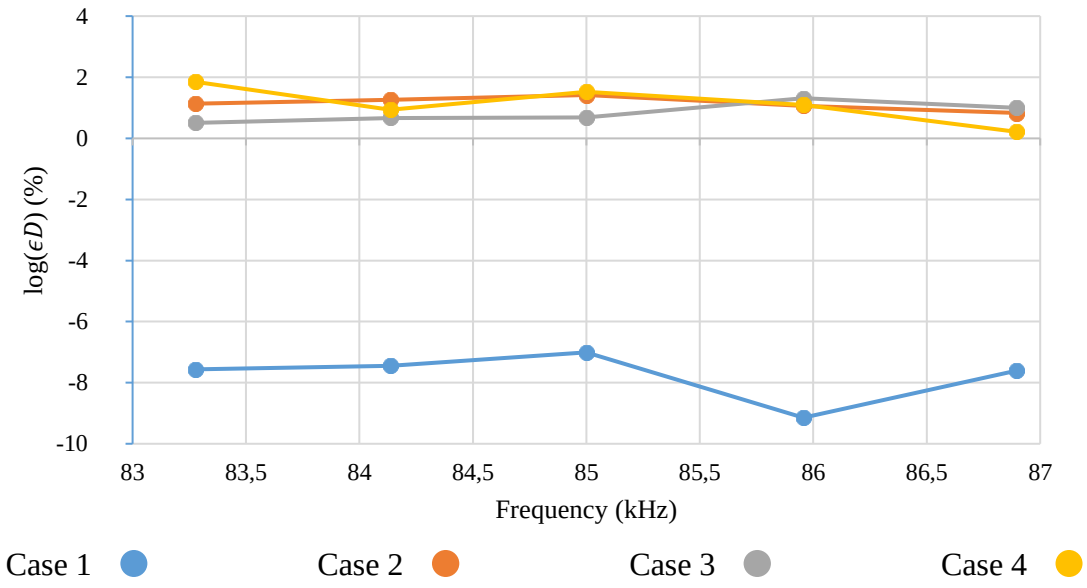

Figure 4.6: Sequent error results of the four experimental cases over the range of frequency from 80 kHz to 90 kHz at 2 A transmitter current

As a result, the experimental measurements prove the theoretical analysis by showing the sequent error values at near zero area, whereas the values at the presence of EMO is much higher, which makes it easy to distinguish the EMO.

For the next procedure, the measurements are done over the spectrum of frequency while maintaining the input power of 10 W. The obtained geometric parameters and the sequent error results are as follows:

$$a = [-0.40182235, 0.1431038, 0.0724854, 1.39473783, -0.58554156]$$

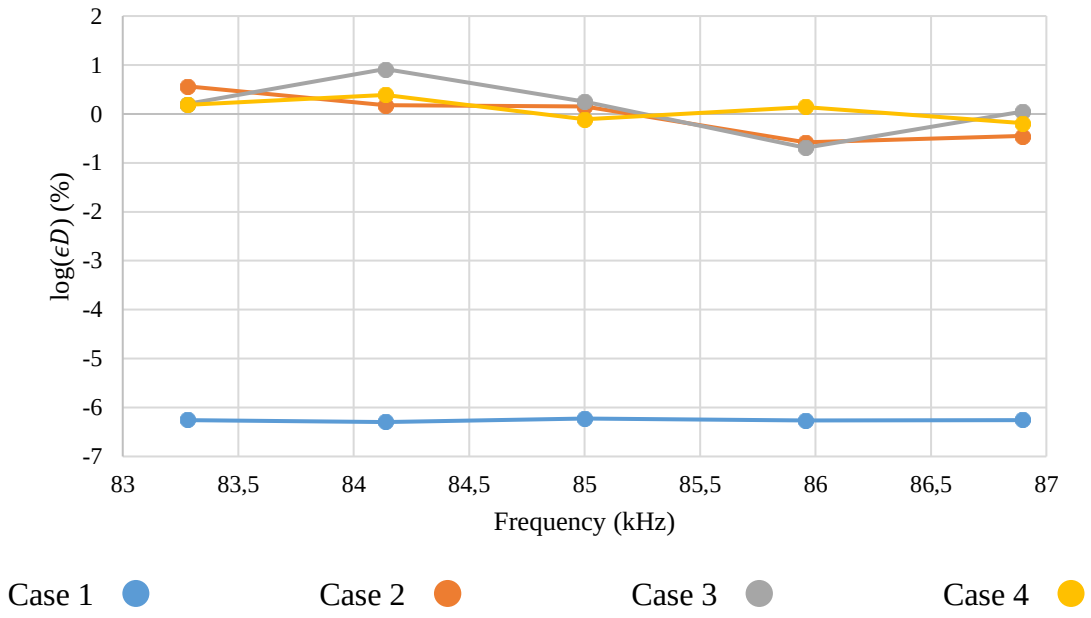

Figure 4.7: Sequent error results of the four experimental cases over the range of frequency from 80 kHz to 90 kHz at 10 W transmitter current

Comparing the results with the previous procedure of the maintained transmitter current of 2 A, it can be seen that even if it is distinguishable whether the EMO is present or not, the difference between the values is more distinct in the procedure with the 2A of transmitter current.

4.4 Localization of the EMO

Additional experimental procedures were performed in terms of localization of the EMO object at different heights and different locations from the center of the systems' operating area. The figure below, demonstrates the measurement points of the experimental setup:

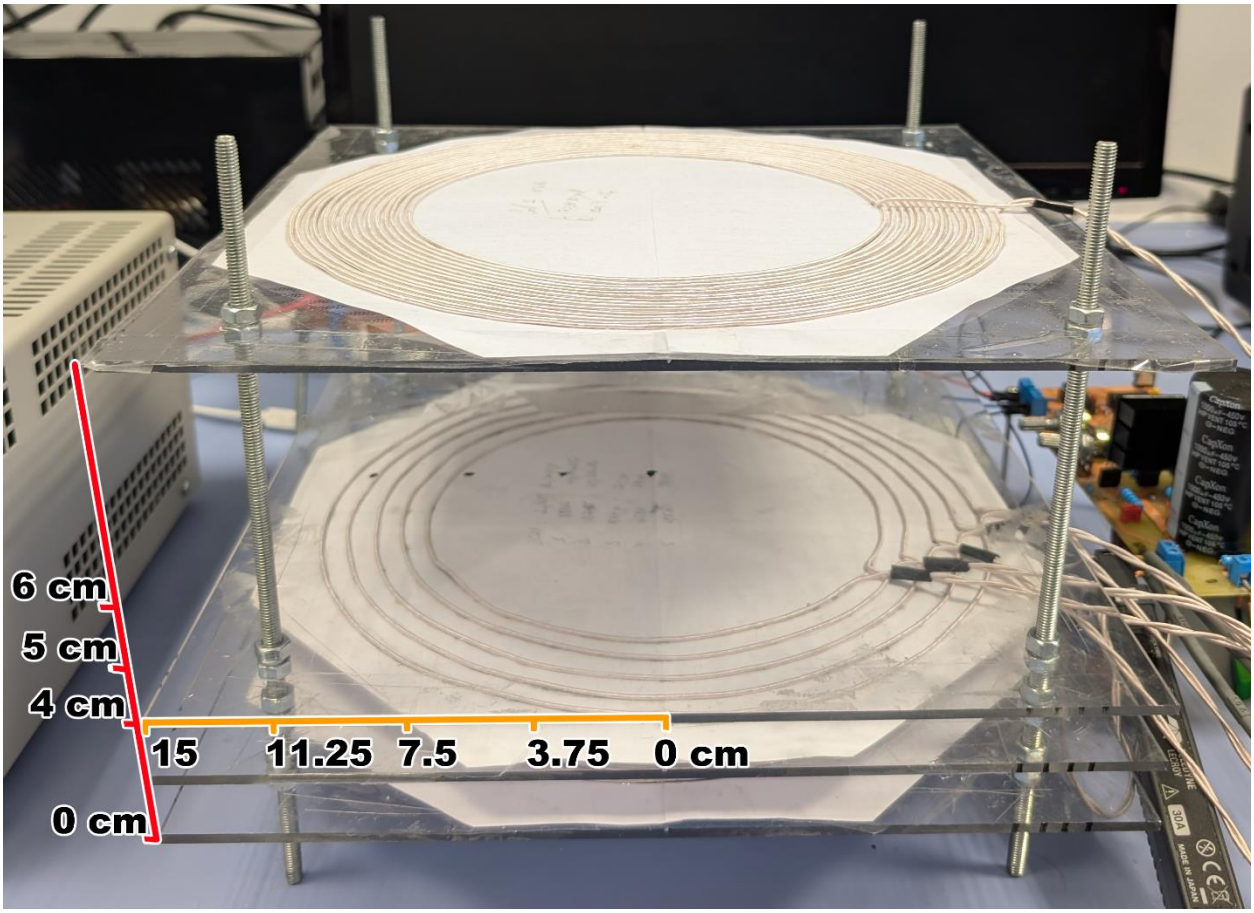

Figure 4.8: Different measuring points of the experimental setup for the localization purposes

The reason for choosing specific points of height in the figure above is due to the usage of tin can as EMO for these experimental measurements and excessive heights levels are not possible. In the Table 4.1, the heatmap of the sequent error is calculated using (3.54) at the different points in the experimental setup and shown as:

Table 4.1. The sequent error values at different points of the experimental setup

ϵD (%)	0 cm	3,75 cm	7,5 cm	11,25 cm	15 cm
6 cm	0,613941	0,101289	1,410979	0,517403	1,372393
5 cm	0,570676	0,393918	0,2314324	0,215687	0,186743
4 cm	1,094192	1,075085	0,9843253	0,060868	1,152817

In Table 4.1, the values are indicated from the white to the red color, which is the lowest to the highest sequent error respectively. By analyzing the values, it can be seen that the at the edge

of the sensing coils and at the lowest height point tin can is less detectable, but as the height point goes up, the closer to the center tin can located the less it is detectable compared to the other points at that height level. Also, it can be pointed out that tin can is identified better at the center when the EMO is at lowest height point compared to the highest point. The reverse happens at the edge of the operating area, where EMO is more detectable at the highest height point compared to the lower points.

Chapter 5 – Discussion

In WPT systems, the suggested sensing coil-based approach for EMO detection shows desirable outcomes, especially in the 80-90 kHz frequency range. The sequent error metric, which is based on differences between measured and reconstructed transmitter currents, accurately detects the presence of EMOs, according to experimental validations and FEA simulations.

5.1 MOD on the Frequency Spectrum

The FEA and experimental findings verify that the operating frequency has a significant impact on the method's accuracy. The sequent error for Case 1 or without EMO in simulations (see Figure 3.10) at the frequency spectrum of 80-90 kHz was closer to 1 %, whereas in the cases with EMO displayed sequent errors in the range from around 70 % to 90 %, with the tin can (Case 3) being more detectable than the other cases.

However, over a wider frequency spectrum from 10 kHz to 1 MHz, the sequent error values of without EMO case is distinguishable yet non-reliable as in the other cases the sequent error linearly rises up to around 500 % with the outlier of around 1000 %. This behavior can be explained due to frequency-dependent effects, including skin effect and eddy current losses.

Additionally, the EOD method was experimentally tested with the first case having constant input power of 10 W and the other case having constant transmitter current of 2 A over the range of frequencies from 83.3 kHz to 86.9 kHz. As a result, constant transmitter current case being better by having lower no EMO case sequent error values and having higher sequent error values of EMO cases compared to the constant power case.

5.2 Sensitivity Analysis on the Parameters of the System

Throughout the studied frequency ranges, it is observed that the self-inductance of transmitter and five sensing coils demonstrated no frequency dependence. This is consistent with

presented Wheeler's formula (3.55), which describes spiral coil self-inductance as geometry-dependent and mainly frequency-independent. It is also confirmed by experimental measurements, where it can be seen that the values stay at the same value with negligible changes occur due to real world possible loose connections.

Regarding self-resistance values across the frequencies, it can be seen that due to the skin effect the value of it increases despite utilizing Litz wires. Additionally, looking at the self-resistance values of transmitter coil, we can observe that the most change is caused by the spoon, which consequently means that the more surface are the MO covers the higher its impact on the self-resistance value of the coils.

5.3 Localization and Spatial Sensitivity

After measuring tin can at different height levels and off-center levels, the sequent error values were calculated. According to the obtained results at the lowest height level of 4 cm above transmitter coil the sequent error values at the near center positions (0 cm and 3.75 cm) are higher than the values at higher heights. However, as the height becomes more, the sequent error values become higher the near edge positions (7.5 cm, 11.25 cm and 15 cm) than the values at the lower heights.

Chapter 6 – Conclusion and Future Work

This thesis introduces a reliable sensing-coil approach for identifying EMOs in WPT systems for EVs, tackling significant safety issues related to overheating hazardous cases caused by eddy currents. The suggested system employs five open-circuited single-turn sensing coils. By measuring the induced voltages in sensing coils and current in transmitter coil, the system can be calibrated and sequent error value can be calculated. The sequent error value is aimed to show the system deviation from the calibrated model, hence indicating EMO in the system. The proposed method operates at a pre-startup power level of 10 W, facilitating safe environmental scanning prior to the initiation of high-power EV charging.

To validate the proposed method, the study combines experimental setup, 3D-FEA performed in Ansys Electronics Desktop software, and theoretical modeling to establish relationships between EMO and coils. Four scenarios of no EMO, a coin, a tin can, and an aluminum spoon were assessed using FEA simulations over frequency ranges of 10 kHz-1 MHz and 80-90 kHz. The findings showed clear sequent error patterns, with errors falling to 1 % in the absence of EMOs and increasing to 70-90 % in their presence. The shorter frequency spectrum from 80 to 90 kHz performed well because at wider frequency ranges instability occurred due to eddy current losses and skin effect, which made it more difficult to calibrate geometric parameters.

The observed changes in coil parameters have shown that the self-inductance values are frequency independent and only affected by the presence of the EMOs, whereas the self-resistance values of the coils are affected by the frequency and the EMOs, which in turn makes self-resistance values affect the calibration process more than the self-inductance values.

The experimental setup performs EOD at 83.3 kHz to 86.9 kHz frequency range with two different cases of having constant transmitter current of 2 A and constant input power of 10 W. As

a result, the maintaining constant transmitter current across the range of frequencies performs better than maintaining 10 W of input power. Additionally, experimental procedures aimed at spatial sensitivity were performed where it was identified that the closer EMO is located to the transmitter coil the better it is detectable at the center of the coil. Inversely, when EMO is located higher from transmitter coil then it is better detection values at the edges of the coil. Spatial sensitivity provided insights towards technique's performance on the real-world scenarios like variable ground clearance and uneven terrain.

Future study may expand upon the analysis on the diverse types of EMOs in terms of how the size or the various material of the EMO affects the system or more identifiable. Also, the proposed method does not distinguish between harmless objects and hazardous ones, which may lead to false positive cases. The previous research on the proposed technique do not address the cases of multiple object scenarios. Testing such cases such as multi-object presence of small metallic objects could reveal useful insights on techniques detection performance. There is still an existing issue with the possible moving objects or objects that may accidentally appear after calibration is done. For such cases, the real time calibration techniques can be proposed to avoid such cases. Additionally, how the various environmental cases such as the presence of dust and water may affect performance of the EOD.

References

[1] P. Lopes, P. Costa and S. Pinto, "Wireless Power Transfer System For Electric Vehicle Charging," 2021 International Young Engineers Forum (YEF-ECE), Caparica / Lisboa, Portugal, 2021, pp. 132-137, doi: 10.1109/YEF-ECE52297.2021.9505094.

[2] S. A. Q. Mohammed and J. -W. Jung, "A Comprehensive State-of-the-Art Review of Wired/Wireless Charging Technologies for Battery Electric Vehicles: Classification/Common Topologies/Future Research Issues," in IEEE Access, vol. 9, pp. 19572-19585, 2021, doi: 10.1109/ACCESS.2021.3055027.

[3] S. Kawasaki, Y. Kobayashi and S. Yoshida, "High-power, high-efficiency microwave circuits and modules for wireless power transfer based on green-Eco technology," 2013 IEEE Radio and Wireless Symposium, Austin, TX, USA, 2013, pp. 28-30, doi: 10.1109/RWS.2013.6486630.

[4] R. Ishikawa and K. Honjo, "Efficient supply power control by PWM technique for microwave wireless power transfer systems," 2014 Asia-Pacific Microwave Conference, Sendai, Japan, 2014, pp. 1101-1103.

[5] N. Shinohara, "Research and standardization activities of wireless power transfer via microwaves at Kyoto university," 2015 International Workshop on Antenna Technology (iWAT), Seoul, Korea (South), 2015, pp. 95-98, doi: 10.1109/IWAT.2015.7365271.

[6] S. Shafiei, S. S. H. Yazdi, M. Kermani, A. Saukhimov, A. Hekmati and M. Bagheri, "Underwater and In-Air IPT-CPT Wireless Power Transfer Performance Comparison: A Simulation Study," 2023 IEEE International Conference on Environment and Electrical Engineering and 2023 IEEE Industrial and Commercial Power Systems Europe (EEEIC / I&CPS Europe), Madrid, Spain, 2023, pp. 1-6, doi: 10.1109/EEEIC/ICPSEurope57605.2023.10194772

[7] D. Rozario, N. A. Azeez and S. S. Williamson, "Analysis and design of coupling capacitors for contactless capacitive power transfer systems," 2016 IEEE Transportation Electrification Conference and Expo (ITEC), Dearborn, MI, USA, 2016, pp. 1-7, doi: 10.1109/ITEC.2016.7520244.

[8] M. Kline, I. Izyumin, B. Boser and S. Sanders, "Capacitive power transfer for contactless charging," 2011 Twenty-Sixth Annual IEEE Applied Power Electronics Conference and Exposition (APEC), Fort Worth, TX, USA, 2011, pp. 1398-1404, doi: 10.1109/APEC.2011.5744775.

[9] D. Kishan and P. S. R. Nayak, "Wireless power transfer technologies for electric vehicle battery charging — A state of the art," 2016 International Conference on Signal Processing, Communication, Power and Embedded System (SCOPES), Paralakhemundi, India, 2016, pp. 2069-2073, doi: 10.1109/SCOPES.2016.7955812.

[10] S. Shafiei et al., "Design and Implementation of Underwater Inductive Power Transfer Systems with an Accurate Eddy Current Loss Model Approach," in IEEE Transactions on Industry Applications, doi: 10.1109/TIA.2024.3524480.

[11] A. Kapanov, A. Almaganbet, S. S. H. Yazdi and M. Bagheri, "Coil Parameters Optimization for Dynamic Wireless Charging of Electric Vehicles using Particle Swarm Optimization (PSO) Algorithm," 2023 International Aegean Conference on Electrical Machines and Power Electronics (ACEMP) & 2023 International Conference on Optimization of Electrical and Electronic Equipment (OPTIM), Istanbul, Turkiye, 2023, pp. 1-7, doi: 10.1109/ACEMP-OPTIM57845.2023.10287037.

[12] M. Lu, M. Bagheri, A. P. James and T. Phung, "Wireless Charging Techniques for UAVs: A Review, Reconceptualization, and Extension," in *IEEE Access*, vol. 6, pp. 29865-29884, 2018, doi: 10.1109/ACCESS.2018.2841376.

[13] A. Junussov, M. Bagheri and M. Lu, "Analysis of magnetically coupled resonator and four-coil wireless charging systems for EV," 2017 International Conference on Sustainable Energy Engineering and Application (ICSEEA), Jakarta, Indonesia, 2017, pp. 1-7, doi: 10.1109/ICSEEA.2017.8267679.

[14] S. S. H. Yazdi, S. Shafiei, A. Kapanov, Y. Shakhin, A. Namadmalan and M. Bagheri, "Enhanced Domino Wireless Power Transfer for Transmission Line Monitoring: Overcoming External Metal Object Interference and Optimizing Coil Design," in IEEE Transactions on Power Delivery, vol. 39, no. 2, pp. 1137-1150, April 2024, doi: 10.1109/TPWRD.2024.3353409.

[15] M.Lu, A.Junussov, and M. Bagheri. “Analysis of resonant coupling coil con f igurations of EV wireless charging system: a simulation study”. In: Frontiers in Energy 14 (Mar. 2019), pp. 152–165. doi: 10.1007/s11708-019-0615-1.

[16] H. Jiang, P. Brazis, M. Tabaddor and J. Bablo, "Safety considerations of wireless charger for electric vehicles — A review paper," 2012 IEEE Symposium on Product Compliance Engineering Proceedings, Portland, OR, USA, 2012, pp. 1-6, doi: 10.1109/ISPCE.2012.6398288.

[17] R. Wiengarten, V. Reising, T. Vosshagen and F. Turki, "About the heating of foreign metallic objects in magnetic field of wireless power transfer by cars," Proceedings of PCIM Europe 2015; International Exhibition and Conference for Power Electronics, Intelligent Motion, Renewable Energy and Energy Management, Nuremberg, Germany, 2015, pp. 1-5.

[18] Y. Tian, W. Guan, G. Li, K. Mehran, J. Tian, and L. Xiang, “A review on foreign object detection for magnetic coupling-based electric vehicle wireless charging,” Green Energy and Intelligent Transportation, vol. 1, no. 2, p. 100007, Sep. 2022, doi: 10.1016/j.geits.2022.100007.

[19] M. Zavrel, V. Kindl and M. Tyrpekl, "Foreign Objects and Living Organism Detection System for the Wireless Power Transfer Active Zone in E-Mobility," IECON 2023- 49th Annual Conference of the IEEE Industrial Electronics Society, Singapore, Singapore, 2023, pp. 1-6, doi: 10.1109/IECON51785.2023.10312095.

[20] C. Herpers and C. D. Rouse, "Lateral Misalignment and Foreign Object Detection in Resonant Capacitive Power Transfer," 2023 IEEE Wireless Power Technology Conference and Expo (WPTCE), San Diego, CA, USA, 2023, pp. 1-5, doi: 10.1109/WPTCE56855.2023.10215924.

[21] S. Li, H. Li, Z. Wu, G. Bao, K. Qian and Y. Li, "Foreign Object Detection for LCC-S Wireless Power Transfer System Based on LSTM," 2021 IEEE International Conference on Emergency Science and Information Technology (ICESIT), Chongqing, China, 2021, pp. 165-169, doi: 10.1109/ICESIT53460.2021.9696918.

[22] Long, M. Han, Q. Zhu and A. P. Hu, "An Online Metal Object Detection Method for Inductive Power Transfer by Improved Dual Frequency Tuning Design," 2023 IEEE Wireless Power Technology Conference and Expo (WPTCE), San Diego, CA, USA, 2023, pp. 1-5, doi: 10.1109/WPTCE56855.2023.10216221.

[23] D. Scher and M. Košík, "Novel Method of Metal Object Detection Based on the Bifurcation Phenomena in Inductive Power Transfer," 2022 Wireless Power Week (WPW), Bordeaux, France, 2022, pp. 567-571, doi: 10.1109/WPW54272.2022.9853970.

[24] J. Wang, J. Gao, A. Yang and J. Zhou, "Impedance Identification-Based Foreign Object Detection for Wireless Power Transfer System," 2022 IEEE 31st International Symposium on Industrial Electronics (ISIE), Anchorage, AK, USA, 2022, pp. 895-898, doi: 10.1109/ISIE51582.2022.9831611.

[25] Y. Zhang, B. Yu, K. Wang, Y. Wang and Y. Yang, "Metal Foreign Object Detection in Electric Vehicle Wireless Power Transmission," 2020 IEEE International Conference on Information Technology, Big Data and Artificial Intelligence (ICIBA), Chongqing, China, 2020, pp. 696-701, doi: 10.1109/ICIBA50161.2020.9277103.

[26] W. Zhong, F. Xiang and C. Hu, "Metal Object Detection With Detection Coils Perpendicular to Power Coils for Wireless Power Transfer Systems," in IEEE Transactions on Power Electronics, vol. 38, no. 9, pp. 10530-10534, Sept. 2023, doi: 10.1109/TPEL.2023.3257019.

[27] X. Wu, Y. Mo, J. Wang, S. Chen, J. Xiao and W. Gong, "Analysis and Design of a Metal Object Detection Method for Wireless Power Transfer Systems," 2023 IEEE 3rd International Conference on Data Science and Computer Application (ICDSCA), Dalian, China, 2023, pp. 286-291, doi: 10.1109/ICDSCA59871.2023.10393736.

[28] T. Zhou, Y. Sun, Y. Lan and K. Song, "Metal Foreign Object Detection Algorithm Based On Multivariate Normal Distribution For Wireless Power Transfer System," 2022 Wireless Power Week (WPW), Bordeaux, France, 2022, pp. 722-727, doi: 10.1109/WPW54272.2022.9901348.

[29] S. Son et al., "Foreign Object Detection of Wireless Power Transfer System Using Sensor Coil," 2021 IEEE Wireless Power Transfer Conference (WPTC), San Diego, CA, USA, 2021, pp. 1-4, doi: 10.1109/WPTC51349.2021.9458010.

[30] W. Gong, J. Wang, J. Xiao, X. Wu, Y. Mo and N. Wu, "Metal Foreign Body Detection in EV WPT Based on Self-Excitation Oscillation," 2023 IEEE 6th International Conference on Automation, Electronics and Electrical Engineering (AUTEEE), Shenyang, China, 2023, pp. 61-65, doi: 10.1109/AUTEEE60196.2023.10408094.

[31] S. Y. Chu, X. Zan and A. -T. Avestruz, "Electromagnetic Model-Based Foreign Object Detection for Wireless Power Transfer," in IEEE Transactions on Power Electronics, vol. 37, no. 1, pp. 100-113, Jan. 2022, doi: 10.1109/TPEL.2021.3100420.

[32] T. Sonnenberg, A. Stevens, A. Dayerizadeh and S. Lukic, "Combined Foreign Object Detection and Live Object Protection in Wireless Power Transfer Systems via Real-Time Thermal Camera Analysis," 2019 IEEE Applied Power Electronics Conference and Exposition (APEC), Anaheim, CA, USA, 2019, pp. 1547-1552, doi: 10.1109/APEC.2019.8721804.

[33] Qi, W. Wang, T. Sun, K. Song, F. Yang and H. Duan, "Research on WPT foreign object detection method based on thermal infrared images," IECON 2022 – 48th Annual Conference of the IEEE Industrial Electronics Society, Brussels, Belgium, 2022, pp. 1-6, doi: 10.1109/IECON49645.2022.9968535.

[34] Y. Tian et al., “Metal object detection for Electric Vehicle Inductive Power Transfer Systems based on hyperspectral imaging,” Measurement, vol. 168, p. 108493, Jan. 2021, doi:10.1016/j.measurement.2020.108493.

[35] S. Y. Chu and A. -T. Avestruz, "Transfer-power measurement: A non-contact method for fair and accurate metering of wireless power transfer in electric vehicles," 2017 IEEE 18th Workshop on Control and Modeling for Power Electronics (COMPEL), Stanford, CA, USA, 2017, pp. 1-8, doi: 10.1109/COMPEL.2017.8013344.

[36] A. Rakhymbay, M. Bagheri and M. Lu, "A simulation study on four different compensation topologies in EV wireless charging," 2017 International Conference on Sustainable Energy Engineering and Application (ICSEEA), Jakarta, Indonesia, 2017, pp. 66-73, doi: 10.1109/ICSEEA.2017.8267689.

[37] J. P. K. Sampath, A. Alphones and D. M. Vilathgamuwa, "Repeater tuning against load variation for wireless power transfer," 2016 IEEE 8th International Power Electronics and Motion Control Conference (IPEMC-ECCE Asia), Hefei, China, 2016, pp. 3173-3177, doi: 10.1109/IPEMC.2016.7512803.

[38] A. Triviño-Cabrera, J. M. González-González, and J. A. Aguado, “Wireless Chargers for Electric vehicles,” Power Systems, pp. 19-41, Sep. 2019. doi:10.1007/978-3-030-26706-3_2.

[39] Nissan Leaf Dimensions 2022- length, width, height, turning circle, ground clearance, wheelbase amp; size. url: https://www.carsguide.com.au/nissan/ leaf/car-dimensions/2022.

[40] K. Aditya and S. S. Williamson, "Design Guidelines to Avoid Bifurcation in a Series–Series Compensated Inductive Power Transfer System," in IEEE Transactions on Industrial Electronics, vol. 66, no. 5, pp. 3973-3982, May 2019, doi: 10.1109/TIE.2018.2851953.

[41] Geoff Klempner; Isidor Kerszenbaum, "Principles of Operation of Synchronous Machines," in Handbook of Large Turbo-Generator Operation and Maintenance , IEEE, 2018, pp.1-52, doi: 10.1002/9781119390718.ch1.